

THESIS FOR THE DEGREE OF DOCTOR OF PHILOSOPHY

Electromagnetic Modeling and Sensitivity-Based Optimization of Medical Devices

by

OSKAR TALCOTH



CHALMERS

Department of Signals and Systems
Biomedical Electromagnetics Group
CHALMERS UNIVERSITY OF TECHNOLOGY
Göteborg, Sweden 2013

Electromagnetic Modeling and Sensitivity-Based Optimization of Medical Devices

OSKAR TALCOTH

ISBN 978-91-7385-951-6

Copyright © OSKAR TALCOTH, 2013.
All rights reserved.

Doktorsavhandlingar vid Chalmers Tekniska Högskola
Ny serie Nr 3633
ISSN 0346-718X

Department of Signals and Systems
Biomedical Electromagnetics Group
Chalmers University of Technology
SE-412 96 Göteborg, Sweden
Telephone: +46 (0)31-772 1000

Front cover: Surface mesh of a cube with images on its faces:

(*upper face*) Parts of a Slurm submit script.

(*left face*) Maxwell's equations.

(*right face*) Amplification of the RF electric field by the presence of an implanted pacemaker system inside a human body phantom in 1.5 T MRI with respect to the empty case. The color scale is logarithmic and covers values from $10^{-0.5}$ to 10^2 .

This thesis has been prepared using L^AT_EX
Printed by Chalmers Reproservice
Göteborg, Sweden, December 2013

Till mamma, pappa och Pernilla

Abstract

Electromagnetics is a fundamental part of biomedical engineering and modern healthcare due to the electromagnetic nature of several important processes in the human body and the interactions of electromagnetic fields with the human body. As a consequence, electromagnetics is exploited for diagnostic and therapeutic purposes by a multitude of medical devices.

The biomedical engineering society strives to develop and design new methods, as well as, to improve existing methods for diagnosis and therapy. In addition, electromagnetic compatibility of both electromagnetic and non-electromagnetic medical devices must be assessed. These tasks can be complicated since electromagnetic measurements in the human body can be difficult and in some cases harmful to the patient. Furthermore, the human body is highly heterogeneous, which makes predictions of its interaction with electromagnetic fields demanding.

In this thesis, these problems are mitigated by means of accurate, unbiased, and automatized electromagnetic modeling that feature a number of disciplines: (i) detailed electromagnetic modeling based on Maxwell's equations; (ii) mathematics with particular emphasis on numerical analysis and optimization; and (iii) large-scale parallel computations on computer clusters. Progress in these three areas enables larger and more difficult problems to be addressed.

In particular, this methodology is applied to three biomedical problems in this thesis. First, the electromagnetics of pacemaker lead heating in MRI is modeled with emphasis on the multi-scale characteristic of the problem. The results show the resonant nature of the problem and that detailed modeling is essential to accurately describe this phenomenon. Second, a method for optimization of sensor positions in magnetic tracking systems is proposed. The method uses powerful mathematics to alleviate the difficulties and computational burden associated with experimental or computational trial-and-error procedures. Third, the estimation procedure in EEG-based source localization is facilitated by exploiting electromagnetic reciprocity during the modeling. This reduces the demands for tailored estimation procedures and removes one obstacle for real-time source localization.

Keywords: Convex optimization, design of experiments, helical conductors, inverse problems, magnetic resonance imaging, magnetic tracking, multi-scale, optimal measurements, optimal sensor placement, MR safety, pacemakers, thin-wire approximation.

Preface

This thesis is for the degree of Doctor of Philosophy at Chalmers University of Technology, Göteborg, Sweden.

The work has been performed in the Biomedical Electromagnetics Group, Department of Signals and Systems at Chalmers between Aug. 2008 and Dec. 2013 under the supervision of Associate Professor Thomas Rylander, Professor Mikael Persson, and Assistant Professor Hoi-Shun Lui. In addition, Prof. Persson acts as examiner of the thesis.

This work has been supported in part by The Swedish Governmental Agency for Innovation Systems (VINNOVA) within the VINN Excellence Center Chase where Micropos Medical, Göteborg and St. Jude Medical, Järfälla, Sweden have been industrial partners.

The work has also been supported by the Swedish National Graduate School in Scientific Computing. Computations were mainly performed on resources at Chalmers Centre for Computational Science and Engineering (C3SE) provided by the Swedish National Infrastructure for Computing (SNIC).

List of Publications

This thesis is based on the work contained in the following papers, referred to in the text by their boldface Roman numerals.

- I. “Monolithic Multi-Scale Modeling of MR-Induced Pacemaker Lead Heating”,
O. Talcoth, T. Rylander, H.S. Lui and M. Persson,
Proceedings of the International Conference on Electromagnetics in Advanced Applications (ICEAA), 2011, pp. 599-602, Torino, Italy, Sept. 12-16, 2011.
- II. “Pacemaker Lead Heating in MRI: Monolithic Multi-Scale Electromagnetic Modeling”,
O. Talcoth and T. Rylander,
In manuscript, 2013.
- III. “Sensor selection in magnetic tracking based on convex optimization”,
O. Talcoth and T. Rylander,
Electronics Letters, Volume 49, Issue 1, pp. 15-16, 2013.
- IV. “Convex optimization of sensor positions in magnetic tracking based on sensor selection”,
O. Talcoth, G. Risting and T. Rylander,
Submitted to Optimization and Engineering, 2013.
- V. “Parameter Scaling in Non-Linear Microwave Tomography”,
P.D. Jensen, T. Rubæk, **O. Talcoth**, J.J. Mohr and N.R. Epstein,
Proceedings of the 2012 Loughborough Antennas & Propagation Conference, Loughborough, United Kingdom, Nov. 12-13, 2012.
- VI. “Evaluation of a Finite-Element Reciprocity Method for Epileptic EEG Source Localization: Accuracy, Computational Complexity and Noise

Robustness”,
Y. Shirvany, T. Rubæk, F. Edelvik, S. Jakobsson, **O. Talcoth**, and M. Persson,
Biomedical Engineering Letters, Volume 3, Issue 1, pp. 8-16, 2013.

Other related publications by the author not included in this thesis:

- **O. Talcoth**, H.S. Lui and M. Persson, “Simulation of MRI-induced heating of implanted pacemaker leads”, *Proceedings of Medicinteknikdagarna 2009*, Västerås, Sweden, Sept. 28-29, 2009.
- **O. Talcoth**, T. Rylander, H.S. Lui and M. Persson, “Optimization of sensor placement in magnetic tracking”, *Proceedings of Medicinteknikdagarna 2010*, Umeå, Sweden, Oct. 6-7, 2010.
- **O. Talcoth**, T. Rylander, H.S. Lui and M. Persson, “MR-induced heating of pacemaker leads: Modeling and simulations”, *Proceedings of Medicinteknikdagarna 2010*, Umeå, Sweden, Oct. 6-7, 2010.
- **O. Talcoth**, T. Rylander, H.S. Lui and M. Persson, “Optimal measurements in magnetic tracking for organ-positioning during radiotherapy”, *Proceedings of Medicinteknikdagarna 2011*, Linköping, Sweden, Oct. 11-12, 2011.
- **O. Talcoth**, T. Rylander, H.S. Lui and M. Persson, “MR-induced heating of pacemaker leads: A parameter study of contributing factors based on multi-scale modeling”, *Proceedings of Medicinteknikdagarna 2011*, Linköping, Sweden, Oct. 11-12, 2011.
- **O. Talcoth** and T. Rylander, “Electromagnetic modeling of pacemaker lead heating during MRI”, Technical report R014/2011, ISSN 1403-266X, Dept. of Signals and Systems, Chalmers University of Technology, Göteborg, Sweden, 2011.
- **O. Talcoth** and T. Rylander, “Optimization of sensor positions in magnetic tracking”, Technical report R015/2011, ISSN 1403-266X, Dept. of Signals and Systems, Chalmers University of Technology, Göteborg, Sweden, 2011.
- **O. Talcoth**, “Electromagnetic modeling and design of medical implants and devices”, Licentiate thesis R016/2011, ISSN 1403-266X, Dept. of Signals and Systems, Chalmers University of Technology, Göteborg, Sweden, 2011.

- **O. Talcoth** and T. Rylander, “Modeling of a multi-scale electromagnetic problem: pacemaker lead heating in MRI”, *Proceedings of AntennEMB 2012*, p. 24, Stockholm, Sweden, Mar. 6-8, 2012.
- **O. Talcoth** and T. Rylander, “Convex optimization of sensor positions for organ-positioning during radiotherapy”, *Proceedings of Medicinteknikdagarna 2012*, Lund, Sweden, Oct. 2-3, 2012.
- **O. Talcoth**, G. Risting and T. Rylander, “Sensitivity Optimization for Electromagnetic Measurement Systems by Sensor Selection”, *Proceedings of 7th European Conference on Antennas and Propagation*, Göteborg, Sweden, Apr. 8-12, 2013.
- **O. Talcoth** and T. Rylander, “A multi-scale electromagnetic model of pacemaker lead heating in MRI”, *Accepted for presentation at AntennEMB 2014*, Göteborg, Sweden, Mar. 11-12, 2014.
- **O. Talcoth**, G. Risting and T. Rylander, “Optimization of sensor positions for a quasi-magnetostatic inverse problem”, *Accepted for presentation at AntennEMB 2014*, Göteborg, Sweden, Mar. 11-12, 2014.

Acknowledgments

There are a number of people to whom I would like to express my sincere gratitude. Without your help and support during the last five years, this thesis - and I - would have been in far worse shape!

My main supervisor and role model **Thomas Rylander** for your guidance, tolerance, calm, patience, knowledge, dedication and outstanding generosity.

My supervisors **Mikael Persson** and **Hoi-Shun Lui** for giving me new perspectives on the scientific and non-scientific parts of life.

Tonny Rubæk and **Yazdan Shirvany** for rewarding cooperation, sharing the ups and downs of research, and - above all - for all the great fun!

Roman Iustin and the Micropos team for believing in me, supporting me, and treating me as one of your own from day one.

Michael Wang with colleagues at St. Jude, for inspiring me with your passion and curiosity.

My master thesis students **Johan Gustafsson**, **Albert Oskarsson**, **Gustav Risting**, **Oscar Rosenstam**, and **Emma Kjellson** for the time and energy you spent, and for pushing me forward.

Erik Abenius and colleagues at Efield, **Daniel Nilsson** and colleagues at C3SE, and the **ITS** crew for all your help.

Kjell Attback for your enthusiasm and encouragement.

Colleagues and **students** at the Dept. of Signals and Systems.

My dear **family** and **friends**, your love and support is invaluable.

OSKAR TALCOTH
Göteborg, Dec. 16, 2013

Contents

Abstract	i
Preface	iii
List of Publications	v
Acknowledgments	ix
Contents	xi
Part I: Introduction	1
1 Introduction	3
1.1 Biomedical engineering	3
1.2 Electromagnetics in biomedical engineering	4
1.3 Overview of the thesis	5
2 Electromagnetic modeling and design	7
2.1 Electromagnetic theory	8
2.2 Computational electromagnetics	10
2.2.1 Volume discretizing schemes	10
2.2.2 Method of moments	13
2.2.3 Errors and validation	15
2.3 Parameter studies, sensitivity analysis and optimization	17
2.4 Inverse problems	18
2.4.1 Definition and properties	18
2.4.2 Assessment of parameter estimation performance	20
2.4.3 Optimization of system design	22

3	Results	25
3.1	Pacemaker lead heating during MRI	25
3.1.1	Background	25
3.1.2	Modeling	27
3.1.3	Results and conclusions	29
3.2	Optimization of sensor positions in magnetic tracking	33
3.2.1	Background	33
3.2.2	Convex optimization based on sensor selection	34
3.2.3	Results and conclusion	36
3.3	A finite-element reciprocity method for EEG source localization	38
3.3.1	Background	38
3.3.2	Modeling	38
3.3.3	Results and conclusion	42
4	Conclusions	45
A	Fields near sharp edges and tips	47
	References	51
Part II:	Publications	61
	Paper I: Monolithic Multi-Scale Modeling of MR-Induced Pacemaker Lead Heating	
	Paper II: Pacemaker Lead Heating in MRI: Monolithic Multi-Scale Electromagnetic Modeling	
	Paper III: Sensor selection in magnetic tracking based on convex optimization	
	Paper IV: Convex optimization of sensor positions in magnetic tracking based on sensor selection	
	Paper V: Parameter Scaling in Non-Linear Microwave Tomography	
	Paper VI: Evaluation of a Finite-Element Reciprocity Method for Epileptic EEG Source Localization: Accuracy, Computational Complexity and Noise Robustness	

Part I

Introduction

Chapter 1

Introduction

1.1 Biomedical engineering

Biomedical engineering is a field of science that positions itself between engineering and medicine and tries to link these two together with the aim of providing improved healthcare. Biomedical engineering is defined as follows by J.D. Bronzino in the introduction and preface of his book on the fundamentals of biomedical engineering [1]:

“Biomedical engineers [.] apply electrical, mechanical, chemical, optical, and other engineering principles to understand, modify, or control biologic (i.e., human and animal) systems, as well as design and manufacture products that can monitor physiologic functions and assist in the diagnosis and treatment of patients.”

Many products and techniques have been produced by and are developed within the biomedical engineering community. A few examples are given in the (non-exhaustive) list below.

- Artificial body parts and organs, e.g., heart-lung bypass machines, artificial heart valves, dialysis machines, respirators, hearing aids.
- Implantable devices such as pacemakers, deep brain stimulators (DBS), and drug delivery systems.
- Artificial limbs and prostheses.
- Medical imaging techniques for diagnostics. For example, X-rays, ultrasound, and magnetic resonance imaging (MRI).
- Linear accelerators for radiotherapy of cancer tumors.

- Electrocardiograms (ECG/EKG) for heart function assessment.
- New biocompatible materials that can be used in the body.
- Computer programs for decision support, information handling etc.
- Tools for robotic surgery, laparoscopic surgery, ablation etc.

1.2 Electromagnetics in biomedical engineering

Electromagnetics can serve to describe several processes in the human body, for example ion transport through cell membranes, conduction of nerve signals, detection of light that impinges on the retina, and muscle stimulation. As a consequence, passive measurements of electromagnetic quantities are exploited. These measurements are performed at low frequencies (kHz and below) since the measured quantities are generated by displacement of ions. For example, the brain is studied by electroencephalography (EEG) and magnetoencephalography (MEG), electrocardiography (ECG/EKG) measures the electrical activity of the heart, and signals in individual nerves can be measured with microneurography.

Furthermore, human body tissue interacts with external electromagnetic fields, which is exploited for imaging purposes. Electromagnetic properties of the tissue can be imaged at low frequencies by impedance tomography and at radio frequencies (RF) by microwave tomography. Static, low frequency, and RF fields are exploited in MRI to image the single proton (^1H) density in the body. As these protons mainly are found as part of water molecules, contrast in MRI images is related to differences in water content, which makes MRI the preferred imaging modality for imaging of soft tissue. At the high end of the frequency scale, X-rays are used to create both projection and tomographic images (computed tomography, CT) of the electron density in the body. Historically, X-rays found its first application in imaging of the skeleton. With the introduction of contrast agents and refinement of X-ray techniques, the applications of X-ray have been extended to also include, for example, soft tissue imaging and imaging of veins and arteries (angiography).

Tissues of the human body do not only interact with electromagnetic fields but they are also affected by the fields, which is exploited in therapeutic applications. Neurostimulators employ low frequency electric fields (pacemakers, implantable defibrillators, deep brain stimulators) or magnetic fields (transcranial magnetic stimulation) in order to affect the nervous system. Radio frequency fields deposit power in body tissues which is used for

destruction of tissue by so-called RF ablation. Furthermore, the outcomes of radio- and chemotherapy of cancer can be improved by heating of the tissue (hyperthermia), which can be microwave-based. Yet higher in frequency, lasers are exploited for numerous purposes including eye surgery. At the high end of the frequency scale, the radiation is able of ionizing atoms. This mechanism forms the foundation of radiotherapy of cancer tumors where cancer cells are destroyed by ionizing radiation.

It should also be noted that techniques exist which, in contrast to the techniques mentioned above, rely on the absence of interaction between human body tissues and applied external fields. For example, static and low frequency magnetic fields are exploited in magnetic tracking where these fields are used for positioning of objects in and around the human body.

In conclusion, electromagnetics has a central role in biomedical engineering and thus in modern healthcare.

1.3 Overview of the thesis

This thesis demonstrates the usefulness and importance of accurate, unbiased, and automatized electromagnetic modeling by means of numerical methods. More specifically, this type of modeling is exploited for biomedical problems.

The thesis consists of two parts. The second part includes the appended publications that form the backbone of this work whereas the first part gives an introduction to the work and the publications.

The first part is divided into four chapters where the first chapter introduces biomedical engineering and the role of electromagnetics in biomedical engineering. In chapter 2, a brief summary of electromagnetic theory is given. Furthermore, computational electromagnetics is introduced and its applications to parameter studies, sensitivity analysis, optimization, and inverse problems are discussed. The theory and methods presented in chapter 2 are then applied to three different biomedical problems: (i) modeling of pacemaker lead heating in MRI; (ii) optimization of sensor positions in magnetic tracking; and (iii) EEG-based source localization. These studies are found among the publications and a summary is given in chapter 3. Finally, the first part ends with chapter 4 where the work is concluded.

Chapter 2

Electromagnetic modeling and design

Mathematical modeling, or simply modeling, is the process of describing a physical situation in terms of mathematical concepts, notation, and language. This description is referred to as a model. Models are fundamental to science as they help scientists to understand, analyse and predict the world around us. Physical laws are models that, in general, have been formulated from and validated against observations, experiments and measurements.

This work is dedicated to electromagnetics. Therefore, an introduction to electromagnetic theory and Maxwell's equations is given in section 2.1 below. Solutions to Maxwell's equations can be found by analytical methods only in certain canonical situations, for example, where the problem geometry features symmetries. Problems that cannot be solved analytically can be addressed with computational methods as introduced in section 2.2 below. The popularity and usefulness of computational techniques is steadily increasing due to the development and improvement of the techniques in themselves, and also due to the, so far, continuous growth in available computing power. As a consequence, computational techniques have come to replace experiments and measurement campaigns in many situations. In addition, computational techniques can provide information on situations where measurements are considered impossible or intractable. For example, measurements of electromagnetic fields in the human body are often avoided due to the associated risk for the subject's health and simulations are exploited instead.

Computational electromagnetics can be exploited for parameter studies, sensitivity analysis, and optimization as introduced in section 2.3 below. Moreover, section 2.4 is devoted to inverse electromagnetic problems for the solution of which computational techniques constitute a valuable tool.

2.1 Electromagnetic theory

Electromagnetic phenomena on a macroscopic scale are described by Maxwell's equations [2]

$$\nabla \times \mathbf{E} = -\frac{\partial \mathbf{B}}{\partial t} \quad (\text{Faraday's law}) \quad (2.1a)$$

$$\nabla \times \mathbf{H} = \frac{\partial \mathbf{D}}{\partial t} + \mathbf{J} \quad (\text{Ampère's law}) \quad (2.1b)$$

$$\nabla \cdot \mathbf{D} = \rho \quad (\text{Gauss' law}) \quad (2.1c)$$

$$\nabla \cdot \mathbf{B} = 0 \quad (\text{Absence of magnetic charges}) \quad (2.1d)$$

where \mathbf{E} is the electric field, \mathbf{B} is the magnetic flux density, \mathbf{H} is the magnetic field, and \mathbf{D} is the electric displacement. Further, \mathbf{J} is the electric current density, ρ is the electric charge density, and t denotes the time.

Moreover, electric charge is conserved

$$\nabla \cdot \mathbf{J} = -\frac{\partial \rho}{\partial t} \quad (2.2)$$

and additional relations between the field quantities are given by the constitutive relations which take the form

$$\mathbf{D} = \varepsilon \mathbf{E} \quad (2.3)$$

$$\mathbf{B} = \mu \mathbf{H} \quad (2.4)$$

in the special case of linear, isotropic, and non-dispersive media. Here, ε is the electric permittivity and μ is the magnetic permeability. The relative permittivity ε_r and the relative permeability μ_r are given by $\varepsilon = \varepsilon_r \varepsilon_0$ and $\mu = \mu_r \mu_0$ where the constants ε_0 and μ_0 are given in table 2.1. Furthermore, in conductive media with conductivity σ , the eddy current density is related to the electric field by $\mathbf{J}_{\text{eddy}} = \sigma \mathbf{E}$ which gives

$$\mathbf{J} = \sigma \mathbf{E} + \mathbf{J}_{\text{ext}} \quad (2.5)$$

where \mathbf{J}_{ext} are impressed currents.

The following boundary conditions can be derived from Maxwell's equations

$$\hat{\mathbf{n}}_2 \times (\mathbf{E}_1 - \mathbf{E}_2) = 0 \quad (2.6a)$$

$$\hat{\mathbf{n}}_2 \cdot (\mathbf{D}_1 - \mathbf{D}_2) = \rho_s \quad (2.6b)$$

$$\hat{\mathbf{n}}_2 \times (\mathbf{H}_1 - \mathbf{H}_2) = \mathbf{J}_s \quad (2.6c)$$

$$\hat{\mathbf{n}}_2 \cdot (\mathbf{B}_1 - \mathbf{B}_2) = 0 \quad (2.6d)$$

Quantity	Value
Speed of light	$c_0 = 299\,792\,458 \text{ m/s}$
Permeability	$\mu_0 = 4\pi \cdot 10^{-7} \text{ Vs/Am}$
Permittivity	$\varepsilon_0 = 1/(c_0^2\mu_0) \approx 8.854 \cdot 10^{-12} \text{ As/Vm}$

Table 2.1: Constants for free space

where the subscripts refer to medium 1 and 2 that are on opposite sides of the boundary, $\hat{\mathbf{n}}_2$ is the outward directed normal of medium 2, and ρ_s and \mathbf{J}_s denote the surface charge density and surface current density on the boundary, respectively.

The scalar and vector potentials ϕ and \mathbf{A} are defined by

$$\mathbf{B} = \nabla \times \mathbf{A} \quad (2.7)$$

$$\mathbf{E} = -\nabla\phi - \frac{\partial\mathbf{A}}{\partial t}. \quad (2.8)$$

Inserting the potentials into Ampère's law (2.1b) and Gauss' law (2.1c), assuming free space conditions ($\varepsilon = \varepsilon_0, \mu = \mu_0, \sigma = 0$) and a time dependence of $\exp(j\omega t)$ where ω is the angular frequency, and exploiting the Lorentz gauge

$$\nabla \cdot \mathbf{A} = -j\omega\varepsilon_0\mu_0\phi \quad (2.9)$$

leads to the vector Helmholtz equation

$$-\left(\nabla^2 + \frac{\omega^2}{c_0^2}\right)\mathbf{A} = \mu_0\mathbf{J}. \quad (2.10)$$

and to the scalar Helmholtz equation

$$-\left(\nabla^2 + \frac{\omega^2}{c_0^2}\right)\phi = \frac{\rho}{\varepsilon_0}, \quad (2.11)$$

respectively.

Maxwell's equations can be solved analytically for certain problems by, for example, separation of variables. Two such problem are the fields in vacuum near (i) a conducting edge, and (ii) the tip of a conducting circular cone, which are treated in appendix A and references [2–4]. These examples are solved with analytical techniques (if we neglect the eigenvalue-type problem in equation (A.5)). However, in many real-life situations, analytical solutions are not available and computational methods must be used instead.

2.2 Computational electromagnetics

Computational electromagnetics include several numerical methods that are based on different approximations. These approximations provide different advantages and drawbacks. Thus, no method is superior to the others for all types of problems. However, one method is almost always better suited than the others for a specific problem. Therefore, the choice of computational method is an important part of the modeling process.

Three popular techniques are discussed below. The finite element method (FEM) and the finite-difference time-domain (FDTD) method are treated in section 2.2.1 whereas the method of moments (MoM) is treated in section 2.2.2. A more thorough introduction to these methods is given in the textbook [3].

The FEM is exploited in **Paper VI** and FDTD is applied in **Paper V**. The MoM is used in **Paper I** and **Paper II** as well as in **Paper III** and **Paper IV**, where a simplified version is exploited.

2.2.1 Volume discretizing schemes

In this section, we present the finite element method and the finite-difference time-domain method. Both these methods rely on a discretization of the computational volume.

The FEM is a computational technique that is widely used within the engineering disciplines for solving linear partial differential equations (PDE) numerically.

Consider the linear PDE

$$L[u] = s \tag{2.12}$$

where L is a linear differential operator, s is a known source term, and $u \in V$ is the unknown function that is to be computed on a domain Ω where V is an appropriate function space, for example a Sobolev space that ensures the integrability of the function and a specified number of its derivatives. (In the following we will use the Lebesgue space L^2 as V for brevity.) This PDE together with suitable boundary conditions on the boundary $\Gamma = \partial\Omega$ form a boundary value problem. Three common types of boundary conditions are:

Dirichlet The solution u is specified on the boundary Γ .

Neumann The derivatives of u are specified on Γ .

Robin A combination of u and its derivatives are specified on Γ .

The FEM consists of the following steps. The computational domain Ω is divided in smaller parts, or *elements*, of simple geometrical shape, for example triangles or quadrilaterals in 2D. The ensemble of elements are referred to as a *mesh*. The solution $u \in V$ is approximated with a linear combination of basis functions $\{\varphi_i\}_{i=1}^n$ as

$$u \approx u_h = \sum_{i=1}^n u_i \varphi_i \in V_h \quad (2.13)$$

where $\{u_i\}_{i=1}^n$ are unknown coefficients and V_h is a finite dimensional subspace of V . Typically, the basis functions are local. For example, a common choice of basis functions is piece-wise linear polynomials. One such basis function is associated with every node in the mesh where it takes the value one whereas it takes the value zero at all other nodes. The approximate solution u_h can of course not be expected to be correct everywhere in Ω since it does not lie in the same function space as u . The FEM computes the approximate solution u_h as the orthogonal projection of u onto V_h . This can also be formulated as putting the residual $r = L[u_h] - s$ to zero in a weighted average (or *weak*) sense. That is,

$$\langle w_j, r \rangle = \int_{\Omega} w_j r d\Omega = \int_{\Omega} w_j (L[u_h] - s) d\Omega = 0 \quad (2.14)$$

for a set of test function $\{w_j\}_{j=1}^n \in V_h$. Here, $\langle \cdot, \cdot \rangle$ denotes an inner product in V which is exemplified with the inner product of L^2 . In the commonly used Galerkin's method, the test functions are chosen to be the functions $\{w_j\}_{j=1}^n = \{\varphi_i\}_{i=1}^n$ that approximate the solution in equation (2.13). Inserting the expansions of u_h and w_j in equation (2.14) leads to a system of linear equations $\mathbf{K}\mathbf{u} = \mathbf{b}$ that can be solved for the unknown coefficients $\mathbf{u} = [u_1, u_2, \dots, u_i, \dots, u_n]^T$. If the basis and test functions are local, as in this example, the system matrix \mathbf{K} is sparse. It can be shown that u_h converges to u as the number of elements n grows for a correctly constructed FEM, that is the subspace V_h tends to V .

For electromagnetic computations where vector quantities are sought, so-called curl-conforming and divergence-conforming basis function are used [5]. Curl-conforming basis functions feature a continuous tangential component over element edges whereas their normal component is allowed to be discontinuous. This ensures that the curl of the basis function is square integrable. In contrast, divergence-conforming basis function feature a continuous normal component over element edges and the tangential component is allowed to be discontinuous. As a consequence, the divergence of the basis function is

square integrable. Furthermore, both curl- and divergence-conforming basis functions are associated with edges/faces instead of nodes in the mesh.

The FEM applied to Maxwell's equations on differential form can handle the presence of inhomogeneous media well since it discretizes the volume of the computational domain. Furthermore, curved boundaries can be well-approximated by the unstructured grids exploited by the method. In addition, this grid type allows for adaptive refinement of the computational domain. Drawbacks of the method include the computational cost associated with solving the (large) system of linear equations. In addition, the FEM exploits implicit time-stepping, in general, if a time domain computation is considered. This is also relatively costly but has the advantage of being unconditionally stable (that is, the method is stable for all choices of step lengths in time).

The FDTD method also exploits Maxwell's equations on differential form. The computational volume is discretized with a Cartesian grid. Thus, different media can be handled well but curved boundaries are represented by "stair-cases". The differential operators are approximated with finite differences in space and a leap-frog scheme in time. This is in contrast to the FEM where the differential operators are left untouched and the solution is approximated instead. As a consequence of discretizing the differential operators, staggered grids are exploited in both time and space. The stability of the method is governed by the Courant-Friedrichs-Lewy (CFL) condition [6, 7] that limits the time step Δt according to

$$\Delta t \leq \frac{1}{c\sqrt{\frac{1}{(\Delta x)^2} + \frac{1}{(\Delta y)^2} + \frac{1}{(\Delta z)^2}}} \quad (2.15)$$

where the size of the grid is denoted by $\Delta x, \Delta y, \Delta z$ in the x -, y -, and z -directions respectively. The CFL condition ensures that a wave in the numerical model can travel at least as quickly as a wave in the physical world. For problems that require a fine spatial discretization, the number of time steps needed can become prohibitively large. The low computational cost in terms of both operations and memory usage, and its ease of implementation, make the FDTD method popular and well-suited for implementation on graphics processing units (GPU).

It should be noted that the FDTD is a special case of the FEM in time domain. If the computational domain is discretized with cubes and Galerkin's method is exploited with edge elements, mass lumping can be achieved by trapezoidal integration. Then, the mass matrix involved in the FEM becomes diagonal which results in the FDTD method [8, 9].

More information on the FEM can be found in references [10, 11] whereas

the FDTD method is treated in more detail in references [12, 13].

2.2.2 Method of moments

The boundary element method is usually referred to as the method of moments (MoM) when applied to electromagnetics. The MoM is based on the integral representations of Maxwell's equations which are usually formulated in frequency domain.

Consider a known electric field \mathbf{E}^{inc} that is incident on a perfectly conducting object Ω_c . The incident field yields induced currents \mathbf{J}_s on the surface of the conductor. These currents radiate a scattered electric field \mathbf{E}^{scat} . The boundary condition in equation (2.6a) implies that

$$\hat{\mathbf{n}} \times (\mathbf{E}^{\text{inc}} + \mathbf{E}^{\text{scat}}) = 0 \quad (2.16)$$

on the boundary $\partial\Omega_c$ of the object with normal $\hat{\mathbf{n}}$. The boundary condition is exploited in the MoM to formulate the electric field integral equation (EFIE) that is solved for the induced surface currents \mathbf{J}_s .

The vector and scalar potentials can now be formed by superposition as

$$\mathbf{A}(\mathbf{r}) = \int_{\partial\Omega_c} G_J(\mathbf{r}, \mathbf{r}') \mathbf{J}_s(\mathbf{r}') dS' \quad (2.17)$$

$$\phi(\mathbf{r}) = \int_{\partial\Omega_c} G_\rho(\mathbf{r}, \mathbf{r}') \rho_s(\mathbf{r}') dS' \quad (2.18)$$

where the Green's functions $G_J(\mathbf{r}, \mathbf{r}')$ and $G_\rho(\mathbf{r}, \mathbf{r}')$ give the vector/scalar potentials at a point \mathbf{r} generated by a "point current"/point charge at \mathbf{r}' , respectively. The Green's functions are given by

$$G_J(\mathbf{r}, \mathbf{r}') = \frac{\mu_0 \exp(-jkR)}{4\pi R} \quad (2.19)$$

and

$$G_\rho(\mathbf{r}, \mathbf{r}') = \frac{1 \exp(-jkR)}{4\pi\epsilon_0 R} \quad (2.20)$$

where $R = |\mathbf{r} - \mathbf{r}'|$ and $k = \frac{2\pi}{\lambda}$.

By inserting (2.17) and (2.18) into equation (2.8) and imposing the boundary condition (2.16), the EFIE is obtained as

$$\begin{aligned} \mathbf{E}_{\text{tan}}^{\text{inc}} &= \frac{j\omega\mu_0}{4\pi} \int_{\partial\Omega_c} \frac{\exp(-jkR)}{R} \mathbf{J}_s(\mathbf{r}') dS' \Big|_{\text{tan}} \\ &+ \frac{j}{4\pi\epsilon_0\omega} \nabla \int_{\partial\Omega_c} \frac{\exp(-jkR)}{R} \nabla' \cdot \mathbf{J}_s(\mathbf{r}') dS' \Big|_{\text{tan}} \end{aligned} \quad (2.21)$$

where ∇' acts on primed (source) coordinates and $\cdot|_{\text{tan}}$ indicates tangential component. A FEM approach with divergence-conforming Rao-Wilton-Glisson (RWG) basis functions [14] is applied to the EFIE. The surface currents \mathbf{J}_s are approximated by a linear combination of the basis functions $\{\mathbf{s}_i(\mathbf{r})\}_{i=1}^N$ as $\mathbf{J}_s \approx \sum_{i=1}^N a_i \mathbf{s}_i(\mathbf{r})$. An integration by parts of the second term of the right hand side of (2.21) together with Galerkin's method lead to a system of linear equation $\mathbf{Z}\mathbf{i} = \mathbf{e}^{\text{incident}}$ that can be solved for the expansion coefficients of the surface currents $\mathbf{i} = [a_1, a_2, \dots, a_N]^T$. Here, the (i, j) :th element of the matrix \mathbf{Z} is given by

$$\begin{aligned} Z_{i,j} = & -\frac{j\omega\mu_0}{4\pi} \int_{\partial\Omega_c} \mathbf{s}_i(\mathbf{r}) \cdot \int_{\partial\Omega_c} \mathbf{s}_j(\mathbf{r}') \frac{\exp(-jkR)}{R} dS' dS \\ & + \frac{j}{4\pi\epsilon_0\omega} \int_{\partial\Omega_c} \nabla \cdot \mathbf{s}_i(\mathbf{r}) \int_{\partial\Omega_c} \nabla' \cdot \mathbf{s}_j(\mathbf{r}') \frac{\exp(-jkR)}{R} dS' dS \end{aligned} \quad (2.22)$$

and the i :th element of $\mathbf{E}_{\text{incident}}$ is given by

$$e_i^{\text{inc}} = - \int_{\partial\Omega_c} \mathbf{s}_i \cdot \mathbf{E}_{\text{tan}}^{\text{inc}} dS. \quad (2.23)$$

Note that, during the assembly of \mathbf{Z} , the $1/R$ singularity from the Green's function can be extracted and integrated analytically leaving a non-singular part for standard numerical integration [15].

In order to avoid problems with internal resonances associated with closed surfaces, the magnetic field integral equation (MFIE) and its linear combination with EFIE, i.e. the combined field integral equation (CFIE), are usually exploited. See the references [3, 10] for more information on these methods.

A widely used approximation is the thin-wire approximation. Consider a perfectly conducting wire of radius a which is thin, i.e. $ka \ll 1$ and introduce a local coordinate system (ξ, Ψ) where ξ describes the position along the wire and Ψ denotes the angle around the circumference of the wire. Furthermore, assume

- (i) that currents flowing in the circumferential direction can be neglected, and
- (ii) that the surface current density flowing along the wire is independent of Ψ .

The surface current density on the wire can now be approximated with a total current $\mathbf{J}_{\text{t.w.}}(\xi) = J_{\text{t.w.}}(\xi)\hat{\xi}$ flowing along the wire as $\mathbf{J}_s(\xi, \Psi) \approx (2\pi a)^{-1} J_{\text{t.w.}}(\xi)\hat{\xi}$. This leads to a reduced number of unknowns and simplifications in the assembly procedure when computing $Z_{i,j}$ in (2.22). Further approximations can be employed but simplifications that remove the

singularity from the Green's function should be avoided since this leads to spurious solutions [3]. Instead, the singularity should be treated by singularity extraction or numerical integration schemes that are suitable for treating logarithmic singularities.

Since only boundaries between different media are discretized in the MoM, the number of unknowns can be substantially reduced as compared with volume discretizing methods if there are few different media. It should also be stressed that radiating boundary conditions are already included in the formulation of the MoM. The price to pay, as compared with volume discretizing methods, is that the system matrix \mathbf{Z} is dense which implies that its inversion comes at a higher computational cost than for a sparse matrix of equal size. In some physical situations, the off-diagonal terms in \mathbf{Z} that describe the interaction between currents represented by different basis functions can be neglected which leads to a much simpler problem. For example, this is exploited in **Paper III** and **Paper IV** where mutual coupling between sensing coils in a quasi-magnetostatic problem is neglected.

2.2.3 Errors and validation

Modeling and numerical computations inherently introduce errors in the computed solution. A fundamental part of the modeling process is to identify the error contributions from different contributing factors and balance them such that the error is minimized for a certain computational cost. Errors can be classified in the categories below [10].

Modeling errors When a real-life situation is described in mathematical terms, many factors are neglected. For example, an antenna that is to be studied might be considered to be surrounded by nothing else than free space although such a situation never occurs in reality.

The mathematical model usually consists of a continuum representation of the problem at hand. The continuum problem is, in general, impossible to solve with analytical methods and numerical methods are exploited instead, which comes at the price of:

Approximation errors Approximations and simplifications such as, for example, the thin-wire approximation described in section 2.2.2, introduce errors. The size of these errors can be estimated by a comparison with computational results that do not exploit the approximation (if they are feasible) as in **Paper II**, or with analytical solutions as in **Paper VI**.

Discretization errors Computational modeling is based on discrete representations of continuous real-world situations. The translation from a continuous to a discrete representation, which is referred to as discretization, introduces errors. Fortunately, these errors depend on the cell size in a predictable way for correctly working computational methods. The size of the errors can therefore be assessed by means of a convergence study that exploits successively finer discretizations, provided that sufficient resources are available for solving the problem with a finer discretization. Furthermore, this allows for extrapolation of the computed result to zero cell size.

An introduction to convergence studies and extrapolation is given in the monograph by Rylander et al. [3] and **Paper I** includes an example of such a study.

Numerical errors Numerical errors are due to the finite precision of computers. These errors are primarily taken into consideration during the design of a computational method. In general, numerical errors contribute less to the total error than the other errors described above as long as the problem is not excessively ill-conditioned.

Thus, the size of errors associated with the solution of continuum problems by computational means can, and should, be assessed.

Assessment of the remaining error type, the modeling errors, is often performed by comparing computational results with measurements of the same physical situation. Since measurements take all influencing factors into account, the measured data is often used as ground truth and the computational model is concluded to be responsible for differences between computed and measured results. However, it is important not to forget that the measured result can be affected by unwanted factors should the measurement setup not be properly designed. Also, great care must be taken to ensure that the same situation is modeled and measured. Differences in modeled and real-life dimensions, positions, material properties etc. can cause a perfectly accurate model to be rejected solely because the measured and modeled situations are not identical.

A computational model with assessed error levels provides the possibility to perform parameter studies, sensitivity analyses, and optimization as described in the following section.

2.3 Parameter studies, sensitivity analysis and optimization

A computational model includes several parameters, e.g. positions, dimensions, and material properties, that affect the solution of the modeled problem. By varying these parameters in a systematic way, their influence on the solution can be understood and assessed. How to vary the parameters is a research branch of its own which is referred to as *design of experiments*. See for example the textbook [16] for an introduction to the field.

Consider a model that computes the value $V(\mathbf{p})$ as a non-linear and non-trivial function of the parameters in $\mathbf{p} \in \Omega_{\mathbf{p}}$. If the number of parameters is small, the computations are relatively cheap, and the parameter space $\Omega_{\mathbf{p}}$ is small in some sense, a study that attempts to exhaustively evaluate the function V for $\mathbf{p} \in \Omega_{\mathbf{p}}$ can be endeavoured. This can be done in a structured or unstructured way by, for example, sampling on a Cartesian grid or at randomly chosen positions in $\Omega_{\mathbf{p}}$, respectively.

However, in many real-life situations an exhaustive study is not possible due to a large number of parameters, expensive computations, and/or a large parameter space. As a consequence, the influence of \mathbf{p} on V can only be investigated in specific parts of the parameter space. Both these types of studies are referred to as *parameter studies*, examples of which are given in **Paper I** and **Paper II**.

In some situations, the influence of \mathbf{p} on V , the *sensitivity*, in and around a certain point $\mathbf{p}_0 \in \Omega_{\mathbf{p}}$ is of interest. The function V is approximated by a linear function by means of a Taylor expansion around \mathbf{p}_0 given by

$$V(\mathbf{p}_0 + \delta\mathbf{p}) \approx V(\mathbf{p}_0) + \nabla_{\mathbf{p}}V(\mathbf{p})\big|_{\mathbf{p}=\mathbf{p}_0} \delta\mathbf{p} + \text{H.O.T.} \quad (2.24)$$

where $\delta\mathbf{p}$ is the deviation from \mathbf{p}_0 and H.O.T. signifies higher-order terms that are neglected. The linear approximation of V is thus, in general, valid only in a neighbourhood around \mathbf{p}_0 , i.e. where the higher-order terms are small in comparison with the constant and linear term.

Derivatives and sensitivities can be computed by means of differentiation of closed-form expressions as demonstrated in **Paper III** and **Paper IV**, finite differences, or solving the adjoint problem as in **Paper V**. They can also be exploited for sensitivity/robustness analyses where the impact of different parameters is assessed and compared, for automated optimization of electromagnetic systems (**Paper III** and **Paper IV**) and for solving inverse problems which is the considered application in **Paper III**, **Paper IV**, **Paper V**, and **Paper VI**.

2.4 Inverse problems

2.4.1 Definition and properties

A *direct* or *forward* problem is a problem where all problem-describing equations and parameters are known. For example, computing the field scattered by a metal sphere with known position and radius in free space that is illuminated by a plane wave with known direction of propagation and frequency.

In contrast, an *inverse* problem consists of estimating one or several problem-describing equations or parameters from (partial) knowledge of the solution to the problem. For the example above, this could consist of estimating the position of the sphere from measurements of the total field at a few specific locations and a limited frequency band.

Frequently encountered inverse electromagnetic problems include the following types:

Source reconstruction/localization Source reconstruction aims at inferring the source position and characteristics from measurements of the electromagnetic fields produced by the source. Source localization is a sub-class of source reconstruction where the characteristics of the source are known and only the position is to be determined. Examples of the latter include magnetic tracking where the position of a transmitter is determined from measurements of the magnetic fields it generates, as discussed in **Paper III** and **Paper IV**, and localization of brain activities from EEG measurements as treated in **Paper VI**.

Reconstruction of constitutive parameters This type of inverse problem consists of determining the permittivity, permeability and conductivity in a bounded region from measurements on its boundary. Electric impedance tomography considers the static and quasi-static electric case. It has been studied for various medical and industrial applications [17] such as, for example, detection of blood clots in the human lungs [18], and detection of twist in wood [19]. The electrodynamic case includes applications like breast-cancer detection [20] and **Paper V**, as well as monitoring of industrial processes [21].

It should be noted that there are more types of inverse problems, for example reconstruction of initial or boundary values, shape reconstruction, and identification of governing equations (system identification).

Inverse problems are, in general, difficult to solve. This is due to their ill-posedness. An ill-posed problem violates one or several of the three criteria for a well-posed problem:

- (i) There exists a solution to the problem.
- (ii) The solution is unique.
- (iii) The solution depends continuously on the data.

For example, violation of the third criterion leads to a problem where a small amount of measurement noise yields to a dramatic change in the obtained solution. This type of ill-posed continuous problem yields an ill-conditioned problem when it is discretized. To overcome the ill-posedness of inverse problems, more *a priori* information can be added, which is called regularization. For example, constitutive parameters that are reconstructed can be restricted to slow spatial variations. Inverse problems are discussed in, for example, the textbook [22].

A common way of formulating and solving an inverse problem is as follows. Consider an inverse problem that aims to determine the problem-describing parameters \mathbf{p} of the forward problem. Establish a model $V^{\text{model}}(\mathbf{p})$ of the measurement system and solve the optimization, or estimation, problem

$$\underset{\mathbf{p}}{\text{minimize}} \quad J[\mathbf{V}^{\text{meas}}, \mathbf{V}^{\text{model}}(\mathbf{p})] \quad (2.25)$$

for the estimate $\hat{\mathbf{p}}$ where the misfit between the measured data V^{meas} and the modeled data V^{model} is quantified by the cost function(-al) J . A popular choice of cost function is different norms such as L^p -norms and the L^2 -norm in particular. Scaling of the data with a weighted norm can be beneficial if, for example, different entries in V^{meas} have different noise characteristics. Another type of scaling is proposed and evaluated in **Paper V**.

Solving an inverse problem is, in general, a complicated task. For example:

- The system model must accurately model the physical system.
- The measurement system must be well-designed due to inverse problems being sensitive to measurement noise.
- The optimization problem must be pertinently defined and efficiently solved.

Especially, these factors influence each other. For example, a very accurate system model might come with a prohibitively large computational cost, etc.

In this work, we address these challenges for different applications. In **Paper VI**, the influence of modeling errors is examined. In addition, the accuracy of several models are compared and their appropriateness for solving the considered problem is investigated. The sensitivity to noise is assessed in **Paper VI** and exploited as a design criterion to be minimized in **Paper III** and **Paper IV**. The two latter papers also propose a method to improve the system design of the measurement system by optimizing its sensor positions. Furthermore, how to formulate the cost function is investigated in **Paper V**.

2.4.2 Assessment of parameter estimation performance

Assessment of the parameter estimation performance is crucial for improvement of a measurement system and comparison between measurement systems. The system model V^{model} is often non-linear in the parameters $\mathbf{p} \in \mathbb{R}^p$ that are to be estimated, which complicates the performance assessment.

Below, we present two performance assessment approaches that are commonly used: (i) linearization; and (ii) full system simulation including nonlinearities. These methods are local for a non-linear problem, i.e. they are valid only for a specific parameter value \mathbf{p}_0 . Therefore, we also discuss different ways of extending local metrics to non-local metrics.

Consider a measurement system that produces N^r measurements $\{V_k^{\text{meas}}\}_{k=1}^{N^r}$. Assume that the measurements consist of a true signal V_k that is corrupted by additive Gaussian measurement noise and that these noise terms are independent and identically distributed. That is,

$$V_k^{\text{meas}}(\mathbf{p}_0) = V_k(\mathbf{p}_0) + n_k, \quad n_k \sim \mathcal{N}(0, \sigma^2) \quad (2.26)$$

where $\mathcal{N}(\mu, \sigma^2)$ denotes the Gaussian distribution with mean μ and variance σ^2 .

With these assumptions, the covariance of the estimated parameters is bounded from below by the so-called Cramér-Rao bound [23]

$$\text{cov } \hat{\mathbf{p}} \succeq \mathbf{M}^{-1} \quad (2.27)$$

for all unbiased estimators. Here, $\mathbf{A} \succeq \mathbf{B}$ signifies that $\mathbf{A} - \mathbf{B}$ is positive semi-definite and $\mathbf{M} \in \mathbb{R}^{p \times p}$ is the so-called Fisher information matrix [24] given by

$$\mathbf{M}(\mathbf{p}_0) = \sum_{k=1}^{N^r} \mathbf{M}_k(\mathbf{p}_0) = \sum_{k=1}^{N^r} \frac{[\nabla_{\mathbf{p}} V_k(\mathbf{p}_0)] [\nabla_{\mathbf{p}} V_k(\mathbf{p}_0)]^T}{\sigma^2}. \quad (2.28)$$

It should be noted that the Cramér-Rao bound can be attained. For example, the bound is attained asymptotically by the maximum-likelihood estimator [23].

In equation (2.28), we see the close connection between the Fisher information matrix and the sensitivities, i.e. the gradient of V with respect to the parameters in \mathbf{p} . Large sensitivities are usually aimed for since they signify that small variations in \mathbf{p} yield large variations in the measured signal V . Equivalently, large sensitivities make the measurement system more robust to noise since large variations in V yield small variations in $\hat{\mathbf{p}}$. Zero sensitivity corresponds to an unchanged measured signal for an infinitesimal change in the underlying parameter. This corresponds to an unidentifiable parameter in the special case with one parameter and one measurement. In the general case, \mathbf{p} is not identifiable if \mathbf{M} is rank-deficient. Since \mathbf{M} is a sum of N^r rank-one matrices,

$$N^r \geq p \quad (2.29)$$

is a necessary but not sufficient condition for \mathbf{p} to be identifiable.

The solutions $\mathbf{q} \in \mathbb{R}^p$ to the equation $\mathbf{q}^T \mathbf{M}(\mathbf{p}_0) \mathbf{q} \leq c$ describe a confidence ellipsoid in the parameter space centered at \mathbf{p}_0 for a certain confidence level described by the constant c . Optimization of a measurement system can aim at minimizing the confidence ellipsoid in some sense. It is convenient, and often necessary [25], to have a scalar metric of performance that is exploited for comparisons between candidate system designs. Therefore, a real-valued criterion function $J(\mathbf{M})$ is usually exploited. Criterion functions are often convex/concave and can be interpreted geometrically. For example, the so-called D-optimality (Determinant-optimal) criterion

$$J_D(\mathbf{M}) = -\log \det(\mathbf{M}) \quad (2.30)$$

is convex on the domain of symmetric positive-definite matrices [26] and it is related to the volume of the confidence ellipsoid. Numerous criteria are available, see for example references [25, 27, 28]. The D-optimality criterion is exploited in **Paper III** and **Paper IV**.

An alternative to the approach based on linearization described above, is to perform a series of full system simulations (or experiments) with random noise for a known \mathbf{p}_0 . By comparing the estimated $\hat{\mathbf{p}}$ with the known \mathbf{p}_0 , statistics can be established that quantify the performance of the parameter estimation. This approach is exploited in **Paper VI**.

The linearization-based method is valid for all unbiased estimators and comes with a low computational cost. However, non-linearities are neglected. In contrast, the method based on full system simulations includes the complete non-linear behaviour of the measurement system. The drawbacks of

this method are that the results are valid only for a specific estimator and that a large number of simulations and estimations must be performed.

Both methods described above are local for a non-linear problem, i.e. they are valid only for a specific \mathbf{p}_0 . However, the performance is usually sought to be assessed in a measurement domain $\Omega_{\mathbf{p}} \subseteq \mathbb{R}^p$. Let the local metric be described by the criterion function $J(\mathbf{M}(\mathbf{p}))$. This metric can be extended to cover the measurement domain in several ways. A straight-forward approach consists of evaluating J at a number of pertinently chosen locations in $\Omega_{\mathbf{p}}$ and build statistics of the results. Below, we consider extensions in an average- and minimax-sense in more detail.

Assume that a prior probability distribution $\pi_{\mathbf{p}}(\mathbf{p})$ for \mathbf{p} that incorporates information about $\Omega_{\mathbf{p}}$ is known. The average, or expected, performance can be computed as

$$J_{\text{EX}} = \mathbb{E}_{\mathbf{p}}\{J(\mathbf{M}(\mathbf{p}))\} = \int_{\mathbb{R}^p} J(\mathbf{M}(\mathbf{p}))\pi_{\mathbf{p}}(\mathbf{p})d\mathbf{p} \quad (2.31)$$

which can be a computationally very expensive task depending on the size of $\Omega_{\mathbf{p}}$ and characteristics of the underlying measurements.

For certain applications, the worst-case performance may be of interest. For example, it might be desired to be able to guarantee a certain level of performance everywhere in the measurement domain. The worst-case performance is quantified by the criterion

$$J_{\text{MMX}} = \max_{\mathbf{p} \in \Omega_{\mathbf{p}}} \{J(\mathbf{M}(\mathbf{p}))\} \quad (2.32)$$

which in itself constitutes an optimization problem that needs to be solved.

It should be noted that extensions of local linear criteria are not truly global since they do not consider the potential presence of local minima in the estimation problem nor do they consider if the parameters can be uniquely estimated everywhere in the measurement domain. More details on these *identifiability* and *estimability* issues are given in [27] and an example of a suggested remedy is given in reference [29].

2.4.3 Optimization of system design

Optimization of a measurement system's design can be formulated as the optimization problem

$$\begin{aligned} & \underset{\Xi}{\text{minimize}} && J(\Xi) \\ & \text{subject to} && \mathbf{p} \in \Omega_{\mathbf{p}} \end{aligned} \quad (2.33)$$

where J is a performance metric, such as the ones discussed in the previous section, and $\Omega_{\mathbf{p}}$ is the measurement domain for which we wish to optimize

the measurements. The design of the measurement system, or the *experiment design*, is denoted by Ξ .

Problems of this type are discussed in the textbooks [23, 27] and from a more mathematical viewpoint in reference [30]. Furthermore, **Paper III** and **Paper IV** are devoted to the optimization of a generic magnetic tracking system by formulating and solving problems of the type in equation (2.33).

Results

3.1 Pacemaker lead heating during MRI

3.1.1 Background

Three different electromagnetic fields that interact with the human body and objects are exploited in MRI (see reference [31] for more details):

Static field The static, or B_0 field, takes high values, e.g. 1.5 T or 3 T, and constitutes the main characteristic of an MRI system. Objects in the static field will be subject to forces and torques. As a consequence, objects risk getting stuck to the MRI system [32] and can be turned into potentially lethal projectiles [33, 34].

Gradient fields The gradient fields are found in the kHz-range and can therefore lead to unwanted nerve stimulation. Metal implants can concentrate the fields and lead to a higher risk of nerve stimulation. Furthermore, these fields can cause metal objects, e.g. wire loops, to vibrate, which can result in strong acoustic noise.

RF field The RF field operates at $\gamma/(2\pi)B_0$ MHz where γ is the gyromagnetic ratio. For protons $\gamma/(2\pi) = 42.58$ MHz/T which leads to an RF frequency of 63.87 MHz for a 1.5 T-system. The RF field causes tissue heating. Therefore, regulatory constraints limit the absorbed power which is measured in W/kg by the specific absorption rate (SAR)

$$SAR = \frac{1}{2} \frac{\sigma |\mathbf{E}|^2}{\rho} \quad (3.1)$$

averaged in space over a certain mass of tissue (1 g, 10 g, whole body, etc.). Here, ρ is the density of the tissue. Conducting implants can lead

to strong electric fields, in particular near sharp edges and corners, that cause important heating. Elongated implants, such as pacemaker and DBS leads, are especially prone to cause severe heating.

Pacemakers and implantable cardioverter-defibrillators (ICDs) as well as MRI are integral parts of modern healthcare. For example, approximately 0.6% of the population had a implanted pacemaker/ICD [35] and 41 MRI examinations per 1000 inhabitants were performed¹ [36] in Sweden in 2012. Similar data led representatives from Medtronic, one of the largest manufacturers of implantable cardiac devices in the world, to estimate a 50 – 75% probability of a patient with such a device being indicated for an MRI examination during the life span of the implanted device [37]. Unfortunately, patients with these devices are not allowed to be examined with MRI due to the interactions of the electromagnetic fields with the implanted device.

Although at least 17 deaths of pacemaker patients related to MRI up to 2007 are reported in reference [38], more than 1400 MRI examinations of pacemaker patients have been performed without any consequences [39], which has led to a debate if specifically designed MR safe pacemakers are needed (see references [40, 41] for a summary). Claims that MRI examinations with necessary precautions and monitoring is safe are opposed by reports of unexpected potentially life-threatening events occurring despite these precautions [42]. Nevertheless, there are currently conditionally MR safe pacemaker systems approved for use in 1.5 T MRI, in the U.S. from one manufacturer and for use in Europe from four manufacturers [40].

It should be stressed that the debate on safe scanning of pacemaker patients with standard devices and the appearance of MR conditional pacemaker systems on the market do not abolish the need for further investigations within this area for at least two reasons: (i) as shown by the aforementioned debate, the behavior of pacemakers in MRI is still hard to predict; and, as a consequence, (ii) the validity of a safety evaluation of a pacemaker system is difficult to assess.

Heating near the electrodes of pacemaker leads is a problematic aspect of the electromagnetic interactions in MRI from a safety perspective [43]. The RF field induces currents in the lead. This yields highly localized electric fields with high field strengths near the tip and ring electrodes, which causes heating by losses in the tissue.

¹This figure is based on data from 14 of Sweden's 18+2 county councils and regions where the county councils/regions comprising the largest hospitals are not included. Therefore, the actual figure is probably higher.

Pacemaker lead heating is difficult to predict due to its dependence on several factors including [44–48]:

- RF frequency and field strength
- Imaging system (coil design, open or closed bore)
- Type and duration of the imaging sequence
- Lead design and length
- Device position and lead configuration within the body
- Type of device (pacemaker, ICD)
- Lead abandoned or attached to a device
- Patient position in the RF coil
- Patient characteristics such as size, body composition, etc.

A summary of the heating impact of different lead design parameters is given in reference [49].

3.1.2 Modeling

In the 1950s, Sensiper [50, 51] exploited analytical techniques to investigate electromagnetic wave propagation on an infinitely long helical conductor. More specifically, the helix is approximated by a cylindrical sheet with anisotropic conductivity. An overview of more recent studies that extend and refine Sensiper’s work is presented in reference [52].

Modeling of the lead heating phenomenon by means of computational techniques is difficult due to three main modeling challenges:

- (i) Variations between examinations in terms of the almost endless combinations of the items listed in the previous section.
- (ii) The heterogeneous nature of the human body with important differences in dielectric properties.
- (iii) The multi-scale geometry which in 1.5 T MRI encompasses length scales from a couple of λ (the human body) to roughly $\lambda/1000$ (small geometrical details of implanted leads).

MOM	Implant model	Surrounding	Purpose
Nyenhuis et al. [31]	Insulated straight wire with one exposed end	Infinite medium	Comparison with measurements
Park [53]	Insulated curved wire with one electrode	Infinite medium	Comparison with measurements
Park et al. [54]	Insulated straight wire with one or two exposed ends	Infinite medium	Determine a lead “transfer function”
Bottomley et al. [46]	Lead with several conductors ^a	Homogeneous phantom	Evaluation of lead designs
FDTD			
Neufeld et al. [55]	Single helix-shaped conductor	Homogeneous phantom	Comparison with measurements
Pisa et al. [56]	Metal box pacemaker unit, insulated curved wire with one bare end	Birdcage coil and anatomical body model	Comparison with guidelines
Mattei et al. [57]	Metal pacemaker unit, insulated curved wire with one bare end	Birdcage coil and anatomical body model	Comparison with measurements
Wilkoff et al. [58]	Experimental	19 anatomical body models, 9 positions in RF coil, 7 RF coils, 1000 lead configurations	Statistical study combined with animal experiments

Table 3.1: Previous modeling

^aModeling details are not specified in reference [46].

Previous modeling is summarized in table 3.1 and has for example addressed inter-examination variations and the heterogeneity of the human body [58] as well as comparison with measurements [55]. However, no modeling in the literature has successfully resolved the small geometrical lead details which have been shown experimentally to have important influence on the heating [46, 59]. Therefore, we exploit the frequency domain MoM to model a heating experiment similar to the one described by the test standard ASTM F2182-09 [60]. Special attention is devoted to the multi-scale aspects of the problem during the modeling. The model includes (i) a generic 16-rung birdcage coil, (ii) a homogeneous body phantom shaped as a rectangular block, and (iii) a highly detailed model of an implanted pacemaker system consisting of a pacemaker unit and a bipolar pacemaker lead with passive fixation. The thin-wire approximation is exploited to model the two conductors of the lead. The model is described in more detail in **Paper I** and **Paper II**. Further, an overview of the modeled geometry is given in figure 3.1.

3.1.3 Results and conclusions

The thin-wire approximation (see section 2.2.2) is exploited for modeling of the conducting wires in the pacemaker lead. The associated discretization and approximation errors (as described in section 2.2.3) are assessed as follows.

In **Paper I**, we propose and evaluate a meshing scheme for helices discretized with straight wire segments where the cross section area is independent of the number of wire segments per helix turn. A convergence study is performed for a single and a double helix illuminated by a plane wave in free space as well as in the MRI setting with birdcage coil and phantom. The study shows that the proposed meshing scheme is superior to a conventional meshing scheme in both convergence order and number of segments per turn that are needed to achieve a certain discretization error.

In **Paper II**, the approximation error of the thin-wire approximation is evaluated by comparing the induced currents on two coaxial helices in free space illuminated by a plane wave for two types of discretization: (i) straight thin-wire segments; and (ii) standard surface discretization with triangular elements. Several helix geometries are studied and bounds are found for the geometry-defining parameters that ensure valid thin-wire results in a qualitative sense. In addition, the discretization scheme from **Paper I** improves the results substantially also in this study. Furthermore, the same setup is exploited to find mesh parameters which ensure that the discretization error caused by the insulation is smaller than the approximation error associated with the thin-wire approximation.

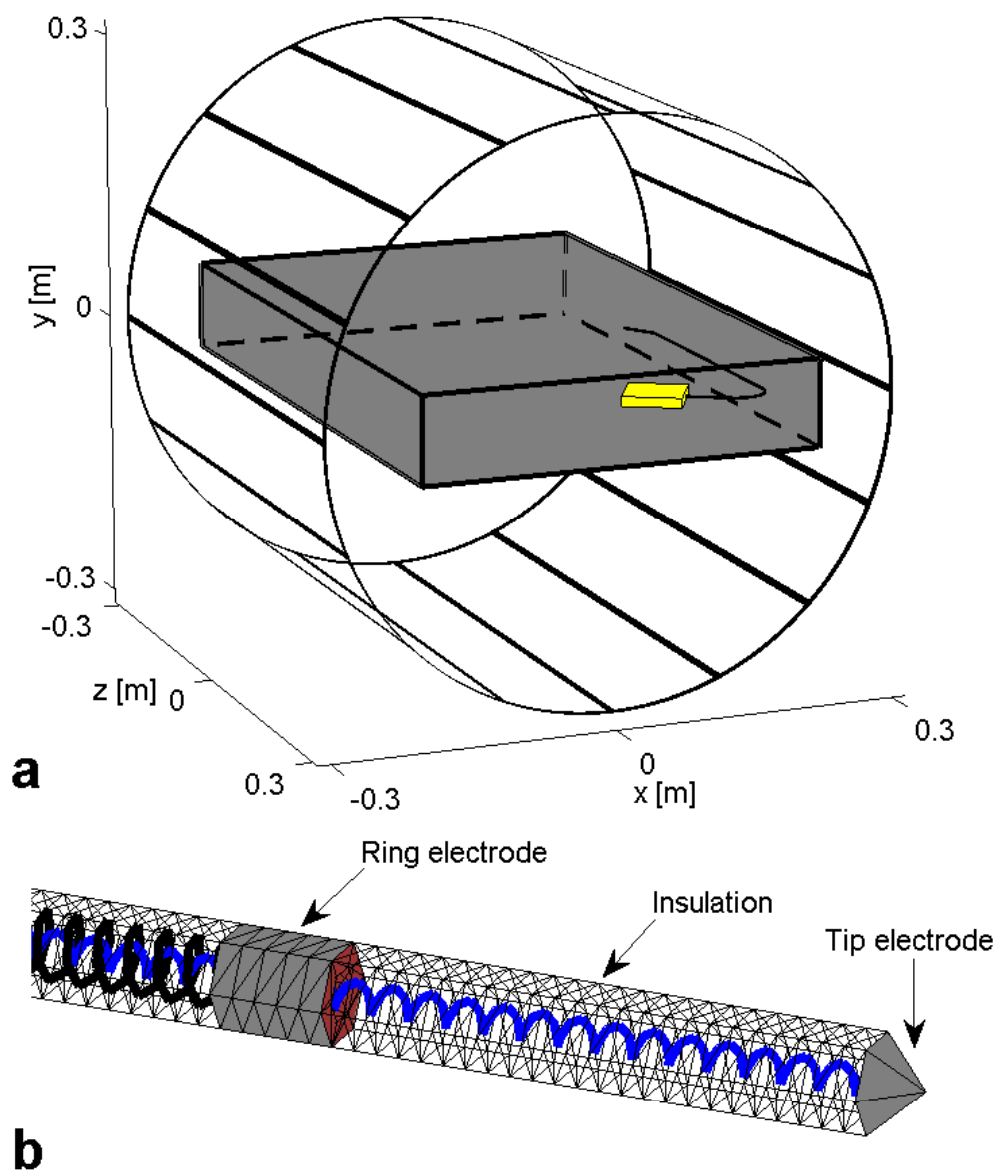


Figure 3.1: **a:** Overview of model geometry with birdcage coil, phantom and implanted pacemaker system. **b:** Distal part of the lead with tip and ring electrodes (*opaque surfaces*), inner (*blue helix*) and outer (*black helix*) conductors, and insulation (*wireframe*).

Having assessed these approximation and discretization errors, the complete model is exploited for an extensive parameter study comprising 425 parameter combinations. For each parameter setting, the induced currents on the conductors as well as the currents flowing into the tip and ring electrodes are evaluated at 53 different frequencies in the range 32 – 128 MHz. The studied parameters are:

- Dielectric properties of the phantom material
- Lead length
- Lead termination including the possible presence of a pacemaker
- Presence of inner and outer conductor
- Conductor characteristics (pitch height, diameter of inner conductor, number of filars, winding direction)
- Lead configuration
- Insulation permittivity and diameter

The results of the parameter study are summarized in **Paper II** and an example is presented in figure 3.2 where the currents induced on the conductors are shown together with the current flowing into the tip and ring electrodes for a straight lead with different lengths. The results clearly show the resonant nature of pacemaker lead heating. Moreover, the resonances change substantially with the following parameters: (i) conductor winding scheme; (ii) conductor length; (iii) conductor inter-turn and inter-conductor distances; (iv) insulation permittivity; (v) lead configuration; and (vi) lead termination including attachment to a pacemaker unit. In particular, the lead heating's dependence on these parameters becomes more chaotic as the conductors are more densely wound. The overall conclusion of **Paper II** is that the small geometrical details of pacemaker leads must be considered if accurate and predictive modeling results are expected.

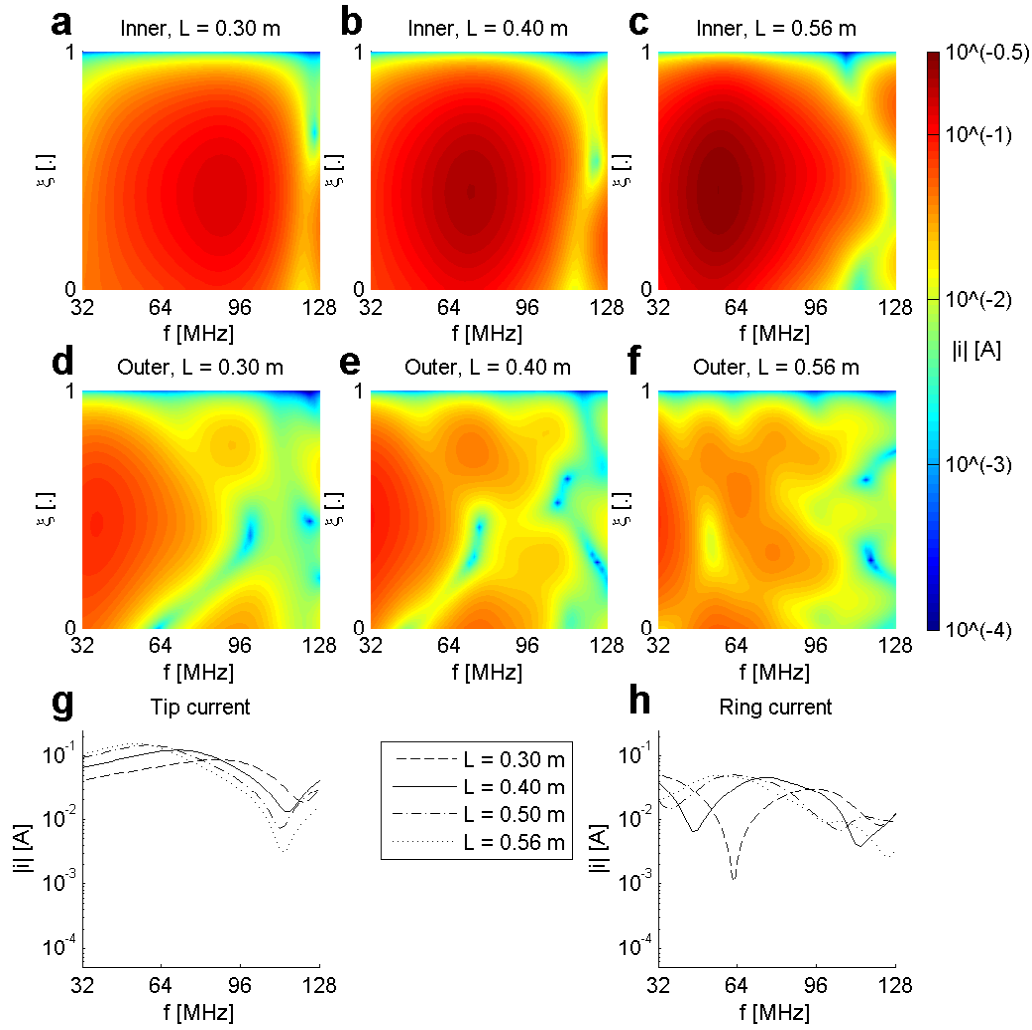


Figure 3.2: Induced inner (a-c) and outer (d-f) conductor currents as well as tip currents (g) and ring currents (h) for different lengths L . The standard implant setup from **Paper II** is exploited with counter-wound conductors. Here, ξ is a normalized coordinate along the conductor.

3.2 Optimization of sensor positions in magnetic tracking

3.2.1 Background

Human body tissue is transparent to static and low-frequency magnetic fields. This is exploited for positioning purposes in and around the human body by so-called *magnetic tracking* systems that determine the position of an object by means of its interaction with the fields mentioned above. Here, we consider a system consisting of an object with unknown position and orientation that transmits a magnetic field and a multitude of sensors or receivers that measures the transmitted field. The position of the transmitter is found as the solution to an inverse source localization problem as discussed in section 2.4.1.

Applications of magnetic tracking include catheter tracking [61, 62], diagnosis of Ménière’s disease by eye tracking [63], real-time organ-positioning during radiotherapy of cancer tumors [64], tracking of wireless capsule endoscopes in the gastro-intestinal tract [65], tracking of tongue movements [66, 67], monitoring of heart valve prostheses [68], estimation of lung segment movements [69], and positioning of bone-embedded implants [70]. Furthermore, magnetic tracking has also been applied for non-medical purposes, such as tracking of the pilot’s head in military aircraft for helmet-mounted sights [71], augmented and virtual reality [72], guidance for underground drilling [73], and tracking of an American football on the pitch [74].

A system model is needed for solving the positioning problem in equation (2.25). A quasi-static approximation of the low-frequency fields is usually exploited. The transmitting and receiving coils can be modeled by magnetic dipoles [68, 71, 75], which is an accurate model at distances that are large in terms of the coil size. A more accurate alternative is offered by models based on the Biot-Savart law such as the one proposed in [63]. Another approach is to construct surrogate models from measurement data instead of modeling the physics, as demonstrated by Justin et al. [64].

The sensor positions of a magnetic tracking system have substantial impact on the tracking accuracy. Previously, Shafrir et al. [76] optimized the sensor positions of a magnetic tracking system by a two-step evolutionary algorithm. Their performance metric is based on a local metric that is computed as a statistic from large numbers of full system simulations. More specifically, the local metric is the root-mean-square value of the error between the true and estimated transmitter positions. The local metric is then considered in a minimax sense over the measurement domain. As a conse-

quence, the computational cost is large and the metric has the drawback of being valid only for a specific positioning algorithm. In contrast, we propose a method that is valid for all unbiased estimators and that does not demand large computations, cf. section 2.4.2.

3.2.2 Convex optimization based on sensor selection

We model a generic quasi-magnetostatic magnetic tracking system in free space that operates at the frequency ω . The coils are modeled as identical magnetic dipoles. The transmitting coil's position \mathbf{r}^t and orientation of the magnetic dipole moment $\hat{\mathbf{m}}^t$ are unknown, i.e., we assume that $\|\mathbf{m}^t\|$ is known. Here, unit vectors are denoted with a hat. In contrast, the positions \mathbf{r}_k^r and orientations $\hat{\mathbf{m}}_k^r$ of the N^r sensing coils are known. Together with Faraday's law (2.1a), this leads to a closed-form expression for the induced voltage in sensor k given by

$$V_k = -j\omega \frac{\alpha \mu_0}{V_0 4\pi} \left(\frac{3(\hat{\mathbf{m}}^t \cdot \mathbf{R}_k)(\hat{\mathbf{m}}_k^r \cdot \mathbf{R}_k)}{R_k^5} - \frac{\hat{\mathbf{m}}^t \cdot \hat{\mathbf{m}}_k^r}{R_k^3} \right) \quad (3.2)$$

where $\mathbf{R}_k = \mathbf{r}_k^r - \mathbf{r}^t$ is the vector from the transmitter to receiving coil k , and $R_k = \|\mathbf{R}_k\|$. Furthermore, V_0 denotes a reference voltage that renders V_k dimension-less and α is a known parameter that models coil characteristics, such as number of turns, diameter, and current flowing in the transmitting coil.

Derivatives of the closed-form expression in equation (3.2) with respect to the transmitter coordinates and orientation-describing parameters in \mathbf{p} can be computed analytically. Thus, the Fisher information matrix (2.28) can also be obtained in closed form. The local D-optimality criterion (2.30) is considered and extended to non-local designs in an average sense

$$J_{\text{ELD}}(\Xi) = -\mathbb{E}_{\mathbf{p}} \{ \log \det \mathbf{M}(\mathbf{p}, \Xi) \} = - \int_{\mathbb{R}^p} \log \det \mathbf{M}(\mathbf{p}, \Xi) \pi_{\mathbf{p}}(\mathbf{p}) d\mathbf{p} \quad (3.3)$$

and in a worst-case sense

$$J_{\text{MMLD}}(\Xi) = \max_{\mathbf{p} \in \Omega_{\mathbf{p}}} \{ -\log \det \mathbf{M}(\mathbf{p}, \Xi) \}. \quad (3.4)$$

Furthermore, we consider bounded measurement domains $\Omega_{\mathbf{p}}$ and a uniform prior distribution $\pi_{\mathbf{p}}(\mathbf{p})$ in $\Omega_{\mathbf{p}}$. The integral in equation (3.3) is approximated by quadrature at the points of the discrete set $\Omega_{\text{lin}} = \{\mathbf{p}_i\}_{i=1}^{N_{\text{lin}}} \subseteq \Omega_{\mathbf{p}}$ with non-negative weights q_i . Trapezoidal quadrature is exploited for the three dimensions of \mathbf{p} that correspond to the transmitter position \mathbf{r}^t . Moreover,

a FEM-inspired quadrature with linear basis functions is used for the two dimensions of \mathbf{p} that correspond to the transmitter orientation $\hat{\mathbf{m}}^t$. (A more detailed description of the quadrature scheme is given in **Paper IV**.) The same set of quadrature points Ω_{lin} is exploited for approximating J_{MMLD} as

$$J_{\text{MMLD}}(\Xi) \approx \max_{\mathbf{p}_i \in \Omega_{\text{lin}}} \{-\log \det \mathbf{M}(\mathbf{p}_i, \Xi)\}. \quad (3.5)$$

It should be noted that J_{ELD} , J_{MMLD} , and their approximations above are convex on the domain of symmetric positive-definite matrices (see **Paper IV**).

The optimization problem in equation (2.33) with either of the cost functions J_{ELD} and J_{MMLD} and an experiment design Ξ consisting of sensor positions is solved by a sensor selection approach based on reference [77], as follows. Instead of optimizing the positions of N^r sensors, the sensor selection aims at finding the best set of N^r sensors among K candidate sensors. This can be formulated as

$$\begin{aligned} & \underset{w_k}{\text{minimize}} && J \left(\frac{1}{N^r} \sum_{k=1}^K w_k \mathbf{M}_k(\mathbf{p}) \right) \\ & \text{subject to} && \mathbf{p} \in \Omega_{\mathbf{p}} \\ & && w_k \in \{0, 1\}, \quad k = 1, \dots, K \\ & && \sum_{k=1}^K w_k = N^r \end{aligned} \quad (3.6)$$

where the weight w_k takes the value one if sensor k is used. As this is a combinatorial problem with $\binom{K}{N^r}$ combinations, exhaustive search is tractable only for small problems.

The difficulties of the combinatorial problem are avoided by modifying the problem slightly. Let each sensor perform N_k measurements and let N_{tot} be the total number of measurements. Introduce the rational number $\lambda_k = N_k/N_{\text{tot}}$. If N_{tot} is large, λ_k can be approximated with a real number, which yields

$$\begin{aligned} & \underset{\lambda_k}{\text{minimize}} && J \left(\sum_{k=1}^K \lambda_k \mathbf{M}_k(\mathbf{p}) \right) \\ & \text{subject to} && \mathbf{p} \in \Omega_{\mathbf{p}} \\ & && 0 \leq \lambda_k \leq 1/p, \quad k = 1, \dots, K \\ & && \sum_{k=1}^K \lambda_k = 1 \end{aligned} \quad (3.7)$$

where the upper bound on λ_k has been introduced to ensure that the condition (2.29) is fulfilled.

If the cost function J is convex on the domain of symmetric positive definite matrices, the optimization problem (3.7) is convex [77], which is the case for J_D , J_{ELD} , and J_{MMLD} . Thus, the problem (3.7) has only one local minimum and the possible multi-modality, i.e. the possible presence of several local minima, is avoided. This is beneficial since multi-modality is a frequently encountered difficulty for this type of problems [25]. Another common difficulty, which is associated with the assumption of uncorrelated noise, is *sensor clusterization* [25]. Sensor clusterization is manifested by optimized solutions where several sensors are located at the same position or very close to each other. A method that merges adjacent sensors is proposed in **Paper IV** to mitigate this problem. As a consequence, the number of sensors in a sensor selection-based solution to the optimization problem (3.7) cannot be imposed beforehand. This is in contrast with the original formulation of the problem.

The sensor selection method is exploited for local designs in **Paper III** and non-local designs in **Paper IV**.

3.2.3 Results and conclusion

Planar sensor arrays are easy to handle due to their limited size which makes this array geometry popular [63, 64]. Therefore, we limit this study to planar sensor arrays although it should be emphasized that the sensor selection method can handle any type of geometry, where sensors could be placed on arbitrary curved surfaces as an example.

First, the sensor selection method is validated against a global optimization method, namely a gradient-based multi-start method. For the considered measurement scenarios, the results in **Paper IV** show that the sensor selection method finds results that are nearly optimal in terms of cost function value and very similar in terms of sensor positions while consuming orders of magnitude smaller computational time.

In **Paper III**, local designs are reported for different \mathbf{p}_0 . For one particular \mathbf{p}_0 where symmetries can be exploited, the problem is also solved by exhaustive search. Showing a relative error of approximately 0.04%, the sensor selection results are in excellent agreement with the results from the exhaustive search.

Non-local designs are investigated in **Paper IV**. The worst performance of the measurement system is obtained for tracking of the transmitting coil in the regions of the measurement domain that are furthest away from the sensor array. This is explained by the strong distance dependence of the

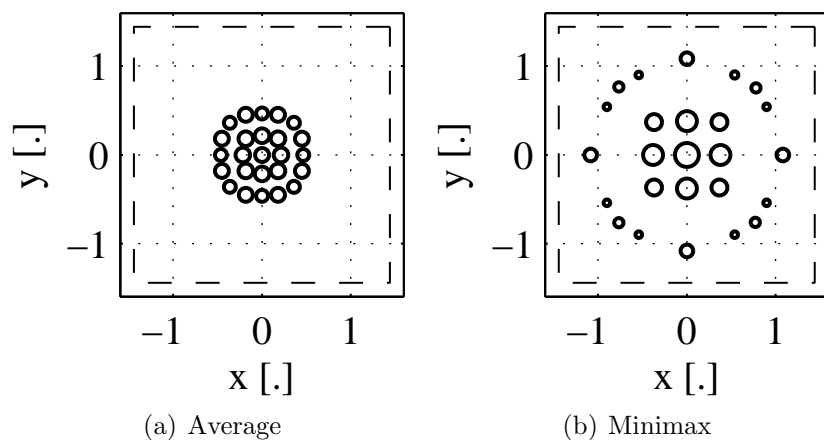


Figure 3.3: Arrays optimized for average optimality (*left*) and minimax optimality (*right*). Selected sensors are represented by circular markers, where the size is proportional to the weight λ_k of the sensor. Sensor array boundaries are indicated with dashed lines.

measured signal (3.2) and its derivatives. As a consequence, sensor arrays that are optimized with the minimax cost function J_{MMLD} are larger than sensor arrays that are optimized with the average cost function J_{ELD} . For example, this can be seen in figure 3.3, where sensor arrays optimized for the average and minimax cost functions are shown. Here, the measurement domain is given by

$$\begin{aligned} \Omega_{\mathbf{p}} = \{ & (x^t, y^t, z^t, \hat{\mathbf{m}}^t) \mid \\ & x^t \in [-0.25, 0.25], \\ & y^t \in [-0.25, 0.25], \\ & z^t \in [0.5, 1], \\ & \hat{\mathbf{m}}^t \in \mathbb{S}^3 \}. \end{aligned} \quad (3.8)$$

where the sensor array lies in the plane $z = 0$, $\hat{\mathbf{m}}^r = \hat{\mathbf{z}}$, and \mathbb{S}^3 denotes the unit sphere in \mathbb{R}^3 .

In essence, optimized arrays, such as the ones in figure 3.3 and in **Paper IV**, are a compromise of two competing desirable features. First, the distance dependence favors sensors that are close to the transmitter and therefore forces the sensors towards the closest position to the measurement domain. Second, the determinant in the cost functions favors sensor arrays where the contributions from the sensors show great diversity. This forces the sensors away from each other.

3.3 A finite-element reciprocity method for EEG source localization

3.3.1 Background

There are several techniques for non-invasive brain activity measurements. For example, functional magnetic resonance imaging (fMRI) measures changes in blood flow that can be related to the activity level of adjacent neurons. Another example is source localization via electroencephalography (EEG). Ion flows associated with nerve signaling create differences in electric potential at the skull surface that can be measured with electrodes. With proper processing of the measured signals, the associated inverse problem can be solved for the source location(s) and/or size. As compared with fMRI, EEG source localization has the advantage of higher temporal resolution.

The EEG source localization problem is similar to magnetic tracking, as discussed previously in section 3.2.1, in that they both can be classified as inverse problems of source localization type (see section 2.4.1). Furthermore, sources are often modeled as dipoles in both cases. However, magnetic tracking is associated with quasi-magnetostatics whereas the EEG source localization problem is a quasi-electrostatic problem. Together with the dielectric properties of human body tissue, this implies that the anatomy of the subject's body must be taken into consideration in EEG source localization. (Remember that the human body is approximated with free space in the magnetic tracking case.)

EEG source localization can serve to identify the location of brain tissue responsible for epileptic seizures, which can be exploited in pre-surgical planning of tissue resection. This is the application in mind for the EEG source localization method that is discussed below and in **Paper VI**.

3.3.2 Modeling

The aim of the forward model is to compute the electric potentials measured by surface electrodes on the scalp due to nerve signals at the position \mathbf{x}_0 inside the brain.

The low frequency nature of nerve signals (kHz and below) permits a quasi-static approximation of Maxwell's equations [78]. Let the computational domain be Ω and let $\mathbf{J} = \mathbf{J}^s + \sigma\mathbf{E}$, where \mathbf{J}^s is the so-called source current. Also, it should be noted that some tissues in the human head are better described by an anisotropic conductivity. If this is taken into account in the model, the conductivity is a tensor instead of a scalar. We limit the discussion below to the isotropic case.

By taking the divergence of equation (2.1b) and noting that the divergence of the curl of a vector field is zero, we obtain Poisson's equation for steady currents

$$\nabla \cdot (\sigma \nabla \phi) = \nabla \cdot \mathbf{J}^s \text{ in } \Omega \quad (3.9)$$

that is solved for the electric potential. We assume that no charge can leave Ω , which is described by the boundary condition

$$\hat{\mathbf{n}} \cdot (\sigma \nabla \phi) = 0 \text{ on } \partial\Omega \quad (3.10)$$

where $\hat{\mathbf{n}}$ is a unit vector that is normal to the boundary. Further, we pick a reference value for the electric potential

$$\phi(\mathbf{x}_{\text{ref}}) = 0 \quad (3.11)$$

for a specified point \mathbf{x}_{ref} in the computational domain.

Since the skull model is obtained from MRI or CT images, we discretize the domain with cubical elements or voxels and apply a finite-element approach with piecewise linear nodal basis functions $\{\varphi_j\}_{j=1}^N$. We expand the potential as $\phi(\mathbf{x}) \approx \sum_{j=1}^N u_j \varphi_j(\mathbf{x})$ and obtain a system of linear equations

$$\mathbf{K}\mathbf{u} = \mathbf{b} \quad (3.12)$$

where $\mathbf{K} \in \mathbb{R}^{N \times N}$ is a sparse symmetric positive definite stiffness matrix with (i, j) :th entry

$$K_{i,j} = \int_{\Omega} \sigma \nabla \varphi_i \cdot \nabla \varphi_j dV, \quad (3.13)$$

$\mathbf{u} \in \mathbb{R}^N$ is the vector with expansion coefficients of the electric potential, and $\mathbf{b} \in \mathbb{R}^N$ is the right hand side vector given by

$$b_j = - \int_{\Omega} \varphi_j \nabla \cdot \mathbf{J}^s dV. \quad (3.14)$$

The reference value for the electric potential in equation (3.11) is incorporated as

$$\phi(\mathbf{x}_{\text{ref}}) = u_{\text{ref}} = 0. \quad (3.15)$$

The electrodes on $\partial\Omega$ (the skull surface) are assumed to measure the potential at a specific node. Usually, the reference value in (3.15) is assigned to one of the electrodes which is referred to as ground.

The source can be modeled as a dipole with dipole moment \mathbf{P} at \mathbf{x}_0 as

$$\mathbf{J}_{\text{dipole}}^s(\mathbf{x}) = \mathbf{P} \delta^3(\mathbf{x} - \mathbf{x}_0) \quad (3.16)$$

where δ is the Dirac delta function and \mathbf{P} is measured in [Am]. This source model has a singularity at \mathbf{x}_0 and is therefore ill-suited for standard FEM. As a consequence, different source modeling methods have been proposed. Here, three of these methods are exploited for modeling of the dipole source:

Direct method The dipole is modeled as a closely spaced current source and current sink with a large current flowing between them [79, 80]. This can be expressed as

$$\nabla \cdot \mathbf{J}^s(\mathbf{x}) = \frac{P}{d} \left[\delta^3 \left(\mathbf{x} - \mathbf{x}_0 - \frac{d}{2} \hat{\mathbf{d}} \right) - \delta^3 \left(\mathbf{x} - \mathbf{x}_0 + \frac{d}{2} \hat{\mathbf{d}} \right) \right] \quad (3.17)$$

where $\mathbf{d} = d\hat{\mathbf{d}}$ is the vector from sink to source, $\mathbf{P} = P\hat{\mathbf{d}} = I_0 d\hat{\mathbf{d}}$ is the dipole moment, and I_0 is the current associated with the source and sink. Inserting this in equation (3.14) yields

$$\begin{aligned} b_j^{\text{dir}} &= -\frac{P}{d} \left[\varphi_j(\mathbf{x}_0 + \frac{d}{2}\hat{\mathbf{d}}) - \varphi_j(\mathbf{x}_0 - \frac{d}{2}\hat{\mathbf{d}}) \right] \\ &= -\frac{P}{d} \left[\nabla \varphi_j(\mathbf{x}_0) \cdot d\hat{\mathbf{d}} + \text{H.O.T.} \right] \end{aligned} \quad (3.18)$$

where a Taylor expansion around \mathbf{x}_0 is exploited and H.O.T signifies higher order terms. Assuming that d is much smaller than the cell size², the higher order terms can be neglected and the right hand side is given by

$$b_j^{\text{dir}} = -\mathbf{P} \cdot \nabla \varphi_j(\mathbf{x}_0). \quad (3.19)$$

Thus, the right hand side contains non-zero entries for the nodes of the element where the source is located.

Subtraction method In the subtraction method [81, 82], the singularity is extracted from the finite element problem by dividing the potential in two parts,

$$\phi = \phi^\infty + \phi^{\text{corr}}. \quad (3.20)$$

Here, ϕ^{corr} is the so-called correction potential and ϕ^∞ is the potential that solves (3.9) for the dipole source in (3.16) in an unbounded homogeneous domain with conductivity σ^∞ . That is

$$\Delta \phi^\infty = \frac{\nabla \cdot \mathbf{J}^s}{\sigma^\infty} \text{ in } \mathbb{R}^3 \quad (3.21)$$

²This can also be expressed as letting $d \rightarrow 0$ as in references [79, 80]. However, it should be noted that, in this case, the dipole moment can no longer be expressed as $\mathbf{P} = I_0 d\hat{\mathbf{d}}$ since this also tends to zero as $d \rightarrow 0$.

which permits a closed form expression for ϕ^∞ ,

$$\phi^\infty = \frac{1}{4\pi\sigma^\infty} \frac{\mathbf{P} \cdot (\mathbf{x} - \mathbf{x}_0)}{|\mathbf{x} - \mathbf{x}_0|^3}. \quad (3.22)$$

Subtracting (3.21) from (3.9) yields the equation

$$\nabla \cdot (\sigma \nabla \phi^{\text{corr}}) = -\nabla \cdot ([\sigma - \sigma^\infty] \nabla \phi^\infty) \text{ in } \Omega \quad (3.23)$$

together with the conditions

$$\hat{\mathbf{n}} \cdot (\sigma \nabla \phi^{\text{corr}}) = -\hat{\mathbf{n}} \cdot (\sigma \nabla \phi^\infty) \text{ on } \partial\Omega \quad (3.24)$$

$$\phi(\mathbf{x}_{\text{ref}}) = 0 \quad (3.25)$$

that can be solved for ϕ^{corr} with the FEM. The system of linear equations

$$\mathbf{K}\mathbf{u}^{\text{corr}} = \mathbf{b}^{\text{sub}} \quad (3.26)$$

features the stiffness matrix given by (3.13) and the right hand side

$$\begin{aligned} b_i^{\text{sub}} &= - \int_{\Omega} \nabla \varphi_i \cdot ([\sigma - \sigma^\infty] \nabla \phi^\infty) dV - \int_{\partial\Omega} \hat{\mathbf{n}} \cdot (\varphi_i \sigma^\infty \nabla \phi^\infty) dS \approx \\ &\approx - \int_{\Omega} \nabla \varphi_i \cdot ([\sigma - \sigma^\infty] \nabla \phi^\infty) dV \end{aligned} \quad (3.27)$$

where it is assumed that the source is sufficiently far away from the boundary so that the boundary term can be neglected due to the strong distance dependence of $\nabla \phi^\infty$. Thus, there is no singularity left in the right hand side provided that $\sigma \rightarrow \sigma^\infty$ when $\mathbf{x} \rightarrow \mathbf{x}_0$ as $\|\mathbf{x} - \mathbf{x}_0\|^\alpha$ where $\alpha > 0$.

In equation (3.27), it can be seen that $b_i^{\text{sub}} \neq 0$ when $\sigma \neq \sigma^\infty$, which leads to a dense right hand side \mathbf{b}^{sub} . To reduce the number of non-zero entries in \mathbf{b}^{sub} , a cut-off function can be exploited that divides the computational domain in two parts such that (i) the subtraction method is exploited around the source, and (ii) the original problem (3.9) is considered in the rest of the domain [83].

Reciprocity-based method Reciprocity is a well-known electromagnetic property in linear time-invariant media with symmetric material property tensors (σ, ϵ, μ) . For the situation studied here, a proof is given in reference [84]. The principle of reciprocity states that the difference in

potential $V_{\alpha\beta}$ between two surface electrodes at \mathbf{x}_α and \mathbf{x}_β caused by a dipole source with dipole moment \mathbf{P} at \mathbf{x}_0 can also be computed as

$$V_{\alpha\beta} = \frac{\mathbf{P} \cdot \mathbf{E}(\mathbf{x}_0)}{I_{\alpha\beta}} \quad (3.28)$$

where \mathbf{E} is the electric field caused by injecting the current $I_{\alpha\beta}$ at electrode α and withdrawing the same current from electrode β . This can be beneficial if a large number of source positions is studied since it suffices to solve the costly model only once for every electrode other than ground with the reciprocity-based method. This should be compared with solving the costly model once for every source position with, e.g., the direct and subtraction methods.

It can also be noted that, as a consequence of reciprocity, the roles of transmitter and receiver can be interchanged in the model (3.2) for the magnetic tracking system studied previously.

3.3.3 Results and conclusion

In **Paper VI**, the reciprocity-based method is compared to the direct and subtraction methods in terms of accuracy and computational speed. Furthermore, the robustness of the reciprocity-based method to noise in the measured signals as well as to modeling errors in the form of electrode misplacement is investigated.

For the assessment of accuracy, a head model consisting of a four-layer sphere was exploited where the layers represent brain tissue, cerebrospinal fluid (CSF), skull, and skin, respectively. Analytical solutions are available for the measured potentials [85]. A comparison of numerical and analytical values is presented in **Paper VI** for dipole sources with tangential and radial orientation as a function of eccentricity, i.e. the distance from the source to the centre of the sphere divided with the radius of the brain-representing sphere. The three source-modeling methods (direct, subtraction, reciprocity-based) yield total errors of similar magnitude. It should be noted that several factors contribute to the total error: (i) source-modeling errors; (ii) discretization errors associated with the discretization of the solution; and (iii) discretization errors associated with the discretization of the geometry, i.e. stair-casing.

Regarding the computational complexity, measurements of the computational time needed for the different parts of the estimation algorithm show that the reciprocity-based method solves the inverse problem in approximately 10^{-4} s. This is roughly four orders of magnitude quicker than the

direct method and six orders of magnitude quicker than the subtraction method. These differences are mainly due to differences in assembly time of the right hand side vector \mathbf{b} , which is, in particular, not needed in the reciprocity-based method.

For the assessment of the reciprocity-based method's robustness to noise, a realistic head model with five tissue types (gray matter, white matter, CSF, skull, scalp) is created by segmentation of MR images. A specific source position is chosen and two orientations (radial and tangential) are considered. Synthetic measurement data created with the subtraction method is corrupted by random noise and the inverse problem is subsequently solved by exhaustive search. For each noise setting, the results are averaged over 500 noise realisations.

Realistic levels of measurement noise (signal to noise ratio between 5 and 10) cause an average localization error of 4.3 mm and 6.3 mm for tangential and radial orientations, respectively.

The importance of minimizing discrepancies between the physical situation that is modeled and the physical situation where measurements are performed is discussed in section 2.2.3. Here, the influence of differences in modeled and measured electrode positions is investigated. For an electrode misplacement of 10 mm, mean localization errors of 4.8 mm and 6.4 mm are obtained for tangential and radial source orientations, respectively.

The localization errors given above are in par with results in the literature and should be compared to the discretization error of 2 mm associated with the computational model.

Chapter 4

Conclusions

Electromagnetics has a central role in biomedical engineering and modern healthcare due to (i) the electromagnetic nature of several important processes in the human body, (ii) the interaction of electromagnetic fields with the human body, and (iii) its usefulness for diagnostic and therapeutic purposes.

In order to address challenging electromagnetic problems within the field of biomedical engineering, this thesis features a powerful methodology that combines (i) detailed electromagnetic modeling by means of Maxwell's equations, (ii) mathematics (e.g. numerical analysis and optimization), and (iii) large-scale parallel computations on computer clusters. Progress in these three areas and, especially, the rapid increase in available computing power continuously enables larger and more difficult problems to be addressed. In this thesis, this methodology is exploited for three important and challenging biomedical problems.

First, the electromagnetics of pacemaker lead heating in MRI is modeled with emphasis on the multi-scale characteristic of the problem. Here, the MoM is exploited and conducting wires are modeled using the thin-wire approximation. A meshing scheme for helical conductors discretized by straight thin-wire segments is proposed and shown to be superior to the conventional approach in terms of both convergence order and error levels. Further, the validity of the thin-wire approximation for closely distanced helical conductors is assessed. A parameter study of the lead heating phenomenon shows the resonant nature of the problem and that detailed modeling is essential to accurately describe this situation.

Second, a method for optimization of sensor positions in magnetic tracking systems is proposed that uses a sensor selection approach and convex optimization to alleviate the difficulties and computational burden associated

with experimental or computational trial-and-error procedures. A comparison with a global optimization method shows that, for the considered measurement scenarios, the proposed method achieves nearly optimal results in terms of cost function value and similar sensor positions in orders of magnitude shorter computational time. Furthermore, important characteristics of the measurement problem are identified and optimized sensor positions are computed for realistic measurement scenarios.

Third, the estimation procedure in EEG-based source localization is facilitated by exploiting electromagnetic reciprocity during the modeling, which reduces the demands for tailored estimation procedures and removes one obstacle for real-time source localization. The proposed modeling approach reduces the computational time of the estimation procedure by several orders of magnitude without sacrificing accuracy as compared with the reference method. Moreover, the sensitivity to measurement noise and sensor misplacement is examined.

In conclusion, this thesis demonstrates that accurate, unbiased, and automatized electromagnetic modeling by means of numerical methods is useful and important for the development of medical devices and advancement of modern healthcare. Fueled by the rapid progress in the constituent areas, this methodology's usefulness, importance, and influence on healthcare will undoubtedly increase in the future.

Fields near sharp edges and tips

Consider the fields in vacuum near: (i) a conducting edge, and (ii) the tip of a conducting circular cone. At distances to the edge/tip that are small compared to the wavelength, the time-dependent problem can be treated as a static one.

First, consider the conducting edge. The problem is treated in 2D where the edge is infinitely long in the z -direction. In the xy -plane, the edge subtends an angle α and, as a consequence, the vacuum region subtends an angle $\beta = 2\pi - \alpha$. The geometry is shown in figure A.1(a). The electric potential ϕ fulfils the Laplace equation with boundary conditions

$$\begin{aligned} \frac{1}{\rho} \frac{\partial}{\partial \rho} \rho \frac{\partial \phi}{\partial \rho} + \frac{1}{\rho^2} \frac{\partial^2 \phi}{\partial \theta^2} &= 0, \quad 0 < \theta < \beta \\ \phi &= V, \quad \theta \in \{0, \beta\} \end{aligned} \quad (\text{A.1})$$

where (ρ, θ) are polar coordinates in the xy -plane and V is a known potential. Separation of variables and determination of constants with the boundary conditions leads to the general solution

$$\phi(\rho, \theta) = V + \sum_{m=1}^{\infty} a_m \rho^{m\pi/\beta} \sin\left(\frac{m\pi\theta}{\beta}\right) \quad (\text{A.2})$$

where the coefficients a_m depend on the potential far away from the edge. Close to the edge, i.e. when ρ is close to 0, the potential can be approximated with only the first term in the sum, that is

$$\phi(\rho, \theta) \approx V + a_1 \rho^{\pi/\beta} \sin\left(\frac{\pi\theta}{\beta}\right) \quad (\text{A.3})$$

from where it can be shown that the components of the electric field as well as the surface charge density at $\theta = 0$ and $\theta = \beta$ vary as $\rho^{\pi/\beta-1}$. Thus, these

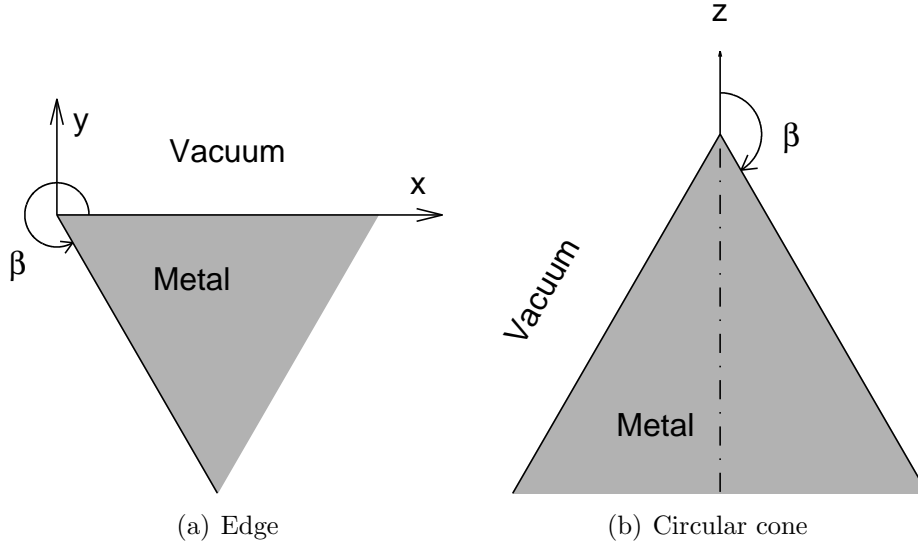


Figure A.1: Two-dimensional edge (*left*) and circular cone (*right*).

quantities are singular for $\beta > \pi$ as $\rho \rightarrow 0$. The most severe singularity occurs when $\beta = 2\pi$, i.e. at the end of a thin sheet, where the fields and charge distribution are proportional to $\rho^{-1/2}$ when $\rho \rightarrow 0$. If the end of a thin sheet with thickness d is rounded, the field strength is proportional to $d^{-1/2}$ at the surface. Details on this derivation are given in the textbooks [2, 3].

Next, consider a conducting cone with circular cross-section that is axially symmetric around the z -axis as shown in figure A.1(b). Let the region defined by $0 \leq \theta < \beta$, where (r, θ, φ) are standard spherical coordinates, be occupied by vacuum. In this region, the electric potential fulfils the Laplace equation. Stating the equation in spherical coordinates, employing separation of variables and the axial symmetry, and exploiting the boundary condition $\phi = 0$ when $\theta = \beta$ gives

$$\phi(r, \theta) = \sum_{k=1}^{\infty} A_k r^{\nu_k} P_{\nu_k}(\cos \theta) \quad (\text{A.4})$$

where A_k are constants, P_{ν} is the Legendre function of the first kind of order ν , and ν_k , $k = 1, 2, 3, \dots$ are the solutions to the eigenvalue-type equation

$$P_{\nu}(\cos \beta) = 0 \quad (\text{A.5})$$

sorted in ascending order. As in the previous example, the sum in equation (A.4) is approximated with its first term for small r , i.e.

$$\phi(r, \theta) \approx A_1 r^{\nu_1} P_{\nu_1}(\cos \theta) \quad (\text{A.6})$$

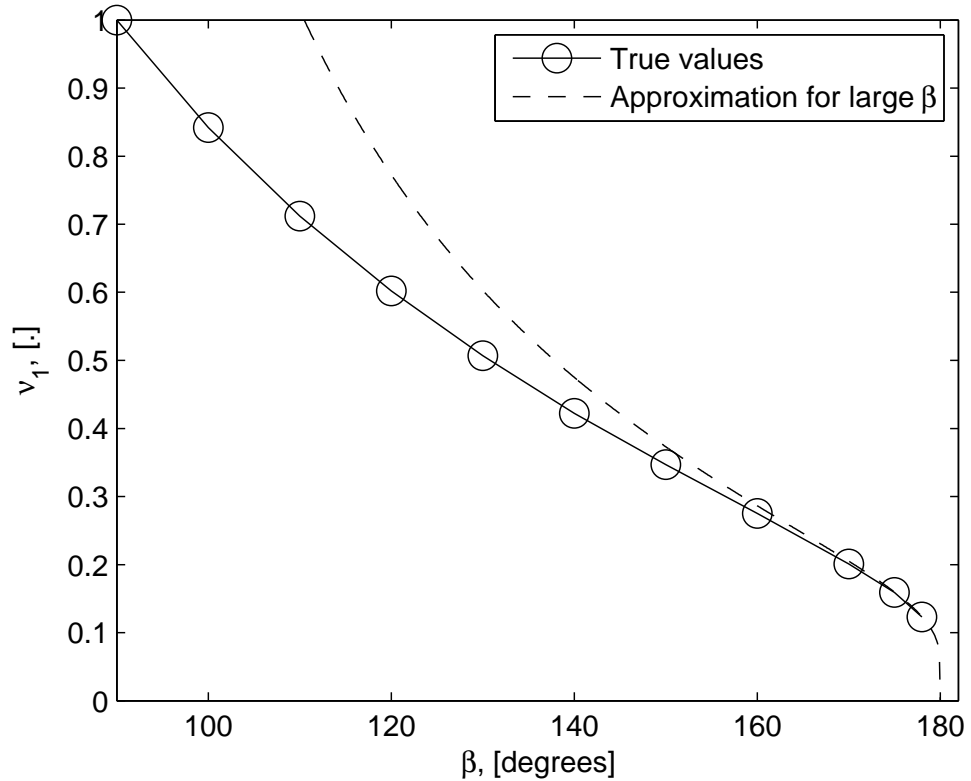


Figure A.2: Smallest root ν_1 of equation (A.5) as a function of β . Values from [4] (*circles, solid*) and the approximation in (A.7) (*dashed*).

from where it can be deduced that the components of the electric field as well as the surface charge density on the cone vary as r^{ν_1-1} when $r \rightarrow 0$. For β close to π , ν_1 can be approximated as

$$\nu_1 \approx \left[2 \log \left(\frac{2}{\pi - \beta} \right) \right]^{-1} \quad (\text{A.7})$$

which is plotted in figure A.2 as a function of β together with values for ν_1 from reference [4] that have been computed as solutions to equation (A.5). For a more detailed derivation of the above, we refer to the textbook [2].

The behaviour of the fields close to the edge and tip described above can be compared to that of the fields close to a line charge, where the fields decay as ρ^{-1} , and close to a point charge, where the fields decay as r^{-2} .

Bibliography

- [1] J.D. Bronzino. *Biomedical Engineering Fundamentals (The Biomedical Engineering Handbook, Third Edition)*. CRC Press, 3rd edition, April 2006.
- [2] J.D. Jackson. *Classical Electrodynamics*. Wiley, 3rd edition, August 1998.
- [3] T. Rylander, A. Bondeson, and P. Ingelström. *Computational Electromagnetics*. Texts in applied mathematics. Springer New York, 2nd edition, 2013.
- [4] J. Van Bladel. Field singularities at the tip of a cone. *Proceedings of the IEEE*, 71(7):901–902, 1983.
- [5] J.C. Nédélec. Mixed finite elements in \mathbb{R}^3 . *Numerische Mathematik*, 35(3):315–341, September 1980.
- [6] R. Courant, K. Friedrichs, and H. Lewy. Über die partiellen Differenzgleichungen der mathematischen Physik. *Mathematische Annalen*, 100(1):32–74, December 1928.
- [7] R. Courant, K. Friedrichs, and H. Lewy. On the partial difference equations of mathematical physics. *IBM journal of Research and Development*, 11:215–234, 1967.
- [8] T. Rylander and A. Bondeson. Stable FEM-FDTD hybrid method for Maxwell’s equations. *Computer Physics Communications*, 125(1-3):75–82, March 2000.
- [9] D.B. Davidson. *Computational Electromagnetics for RF and Microwave Engineering*. CUP, 2005.

- [10] A.F. Peterson, S.L. Ray, and R. Mittra. *Computational Methods for Electromagnetics*. IEEE Press, New York, NY, 1997.
- [11] J.M. Jin. *The Finite Element Method in Electromagnetics*. John Wiley & Sons, New York, NY, 1993.
- [12] K.S. Yee. Numerical solution of initial boundary value problems involving Maxwell's equations in isotropic media. *IEEE Transactions on Antennas and Propagation*, 14(3):302–307, May 1966.
- [13] A. Taflove and S. Hagness. *Computational Electrodynamics: The Finite-Difference Time-Domain Method*. Artech House, Norwood, MA, 3rd edition, 2005.
- [14] S. Rao, D. Wilton, and A. Glisson. Electromagnetic scattering by surfaces of arbitrary shape. *IEEE Transactions on Antennas and Propagation*, 30(3):409–418, May 1982.
- [15] R.D. Graglia. On the numerical integration of the linear shape functions times the 3-D Green's function or its gradient on a plane triangle. *IEEE Transactions on Antennas and Propagation*, 41(10):1448–1455, 1993.
- [16] D.C. Montgomery. *Design and Analysis of Experiments*. John Wiley & Sons, 2006.
- [17] D.S. Holder. *Electrical Impedance Tomography: Methods, History and Applications*. Series in Medical Physics and Biomedical Engineering. Institute of Physics Publishing, Bristol, 2005.
- [18] M. Cheney, D. Isaacson, and J.C. Newell. Electrical Impedance Tomography. *SIAM Review*, 41(1):85–101, January 1999.
- [19] B. Nilsson, T. Sjöden, S. Nordebo, and H. Säll. A method for under-bark detection of the wood grain angle radial dependence. *Wood Material Science and Engineering*, 2(3-4):118–129, September 2007.
- [20] T.M. Grzegorzcyk, P.M. Meaney, P.A. Kaufman, R.M. DiFlorio-Alexander, and K.D. Paulsen. Fast 3-D tomographic microwave imaging for breast cancer detection. *IEEE transactions on medical imaging*, 31(8):1584–92, August 2012.
- [21] L. Cerullo. *Microwave measurement systems for in-line 3D monitoring of pharmaceutical processes*. PhD thesis, Chalmers University of Technology, Göteborg, Sweden, 2013.

-
- [22] R.C. Aster, B. Borchers, and C.H. Thurber. *Parameter estimation and inverse problems*. Elsevier Academic Press, 1st edition, 2005.
- [23] É. Walter and L. Pronzato. *Identification of parametric models from experimental data*. Communications and control engineering. Springer, 1997.
- [24] S.M. Kay. *Fundamentals of Statistical Signal Processing: Estimation Theory*. Number v. 1 in Prentice Hall Signal Processing Series. Prentice-Hall PTR, 1993.
- [25] D. Ucinski. *Optimal measurement methods for distributed parameter system identification*. CRC Press LLC, Boca Raton, 2005.
- [26] S. Boyd and L. Vandenberghe. *Convex optimization*. Cambridge University Press, UK, 2004.
- [27] L. Pronzato and A. Pázman. *Design of experiments for nonlinear models*. Springer New York, 2013.
- [28] A.C. Atkinson, A.N. Donev, and R. Tobias. *Optimum experimental designs, with SAS*, volume 34. Oxford University Press, USA, 2007.
- [29] A. Pázman and L. Pronzato. Extended Optimality Criteria for Optimum Design in Nonlinear Regression. In D. Ucinski, A.C. Atkinson, and M. Patan, editors, *mODa'10 - Advances in Model-Oriented Design and Analysis, Proceedings of the 10th Int. Workshop, Contributions to Statistics*, pages 195–202, Heidelberg, 2013. Springer International Publishing.
- [30] F. Pukelsheim. *Optimal design of experiments*. Classics in applied mathematics. SIAM/Society for Industrial and Applied Mathematics, 2006.
- [31] J.A. Nyenhuis, R. Kamondetdacha, A. Amjad, F.G. Shellock, and A.R. Rezai. MRI and implanted medical devices: basic interactions with an emphasis on heating. *IEEE Transactions on Device and Materials Reliability*, 5(3):467–480, September 2005.
- [32] M. NessAiver. Simply Physics - Flying Objects. www.simplyphysics.com/flying_objects.html, Accessed Oct. 4, 2011.
- [33] R.C. Archibold. Hospital Details Failures Leading to M.R.I. Fatality. www.nytimes.com/2001/08/22/nyregion/hospital-details-failures-leading-to-mri-fatality.html?src=pm, Accessed Oct. 4, 2011, Published Aug. 22, 2001.

- [34] M.F. Dempsey, B. Condon, and D.M. Hadley. MRI safety review. *Seminars in ultrasound, CT, and MR*, 23(5):392–401, October 2002.
- [35] F. Gadler. Annual Statistical Report 2012 - Swedish ICD and Pacemaker Register. Technical report, Karolinska Hospital, Department of Cardiology, Stockholm, Sweden, 2012.
- [36] Nysam. Nyckeltal 2012, Rapport, Röntgen. Available at: www.nysam.com/rapporter.aspx, 2012.
- [37] R. Kalin and M.S. Stanton. Current clinical issues for MRI scanning of pacemaker and defibrillator patients. *Pacing and clinical electrophysiology : PACE*, 28(4):326–8, April 2005.
- [38] E.T. Martin and D.A. Sandler. MRI in patients with cardiac devices. *Current cardiology reports*, 9(1):63–71, March 2007.
- [39] J.F. Zikria, S. Machnicki, E. Rhim, T. Bhatti, and R.E. Graham. MRI of patients with cardiac pacemakers: a review of the medical literature. *AJR. American journal of roentgenology*, 196(2):390–401, February 2011.
- [40] F.Z. Ahmed, G.M. Morris, S. Allen, R. Khattar, M. Mamas, and A. Zaidi. Not all pacemakers are created equal: MRI conditional pacemaker and lead technology. *Journal of cardiovascular electrophysiology*, 24(9):1059–65, September 2013.
- [41] J.R. Gimbel. Computer modeling and MRI-device safety: Modeling, myths, and magical thinking. *Heart Rhythm*, pages 108–109, October 2013.
- [42] J.R. Gimbel. Unexpected asystole during 3T magnetic resonance imaging of a pacemaker-dependent patient with a 'modern' pacemaker. *Europace*, 11(9):1241–2, September 2009.
- [43] M.J.W. Götte, I.K. Rüssel, G.J. de Roest, T. Germans, R.F. Veldkamp, P. Knaapen, C.P. Allaart, and A.C. van Rossum. Magnetic resonance imaging, pacemakers and implantable cardioverter-defibrillators: current situation and clinical perspective. *Netherlands heart journal*, 18(1):31–7, January 2010.
- [44] J.L. Helfer. MRI Safety Update: RF Induced Heating. www.biophan.com/index.php?option=com_docman&task=doc_download&gid=23, Accessed Oct. 5, 2011, Published 2006.

- [45] D.A. Langman, I.B. Goldberg, J.P. Finn, and D.B. Ennis. Pacemaker lead tip heating in abandoned and pacemaker-attached leads at 1.5 Tesla MRI. *Journal of Magnetic Resonance Imaging*, 33(2):426–31, February 2011.
- [46] P.A. Bottomley, A. Kumar, W.A. Edelstein, J.M. Allen, and P.V. Karmarkar. Designing passive MRI-safe implantable conducting leads with electrodes. *Medical Physics*, 37(7):3828–3843, 2010.
- [47] E. Mattei, G. Calcagnini, M. Triventi, F. Censi, and P. Bartolini. Numerical FDTD models of electromagnetic field generated by the RF coil of an MRI scanner: comparison among different solutions. In *Proceedings of the Sixth IASTED International Conference on Biomedical Engineering*, pages 187–192. ACTA Press, 2008.
- [48] P. Nordbeck, I. Weiss, P. Ehses, O. Ritter, M. Warmuth, F. Fidler, V. Herold, P.M. Jakob, M.E. Ladd, H.H. Quick, and W.R. Bauer. Measuring RF-induced currents inside implants: Impact of device configuration on MRI safety of cardiac pacemaker leads. *Magnetic Resonance in Medicine*, 61(3):570–8, March 2009.
- [49] O. Talcoth. Electromagnetic modeling and design of medical implants and devices, R016/2011. Technical report, Dept. Signals and Systems, Chalmers Univ. of Tech, Göteborg, Sweden, 2011.
- [50] S. Sensiper. Electromagnetic Wave Propagation on Helical Conductors. Technical report, Massachusetts Institute of Technology, Cambridge, 1951.
- [51] S. Sensiper. Electromagnetic Wave Propagation on Helical Structures (A Review and Survey of Recent Progress). *Proceedings of the IRE*, 43(2):149–161, 1955.
- [52] G. Naveen Babu. *Electromagnetic Wave Propagation in Anisotropically Conducting Tape Helix Slow Wave Structures*. PhD thesis, Jaypee Institute of Information Technology, 2013.
- [53] S.M. Park. *MRI safety: Radiofrequency field induced heating of implanted medical devices*. PhD thesis, Purdue University, West Lafayette, Indiana, USA, 2006.
- [54] S.M. Park, R. Kamondetdacha, and J.A. Nyenhuis. Calculation of MRI-induced heating of an implanted medical lead wire with an electric field

- transfer function. *Journal of Magnetic Resonance Imaging*, 26(5):1278–1285, 2007.
- [55] E. Neufeld, S. Kühn, G. Szekely, and N. Kuster. Measurement, simulation and uncertainty assessment of implant heating during MRI. *Physics in medicine and biology*, 54(13):4151–69, July 2009.
- [56] S. Pisa, P. Bernardi, M. Cavagnaro, and E. Piuzzi. Power Absorption and Temperature Elevation Produced by Magnetic Resonance Apparatus in the Thorax of Patients With Implanted Pacemakers. *IEEE Transactions on Electromagnetic Compatibility*, 52(1):32–40, February 2010.
- [57] E. Mattei, G. Calcagnini, F. Censi, M. Triventi, and P. Bartolini. Numerical model for estimating RF-induced heating on a pacemaker implant during MRI: experimental validation. *IEEE transactions on bio-medical engineering*, 57(8):2045–52, August 2010.
- [58] B.L. Wilkoff, T. Albert, M. Lazebnik, S.M. Park, J. Edmonson, B. Herberg, J. Golnitz, S. Wixon, J. Peltier, H. Yoon, S. Willey, and Y. Safriel. Safe MRI Scanning of Patients with Cardiac Rhythm Devices: A Role for Computer Modeling. *Heart Rhythm*, October 2013.
- [59] E. Mattei, G. Calcagnini, F. Censi, M. Triventi, and P. Bartolini. Role of the lead structure in MRI-induced heating: In vitro measurements on 30 commercial pacemaker/defibrillator leads. *Magnetic Resonance in Medicine*, 67(4):925–35, April 2012.
- [60] *Standard Test Method for Measurement of Radio Frequency Induced Heating Near Passive Implants During Magnetic Resonance Imaging, Standard F2182-09*. ASTM International, West Conshohocken, PA, USA, 2010.
- [61] S. Krueger, H. Timinger, R. Grewer, and J. Borgert. Modality-integrated magnetic catheter tracking for x-ray vascular interventions. *Physics in Medicine and Biology*, 50(4):581–597, February 2005.
- [62] Biosense Webster. Carto 3 System. www.biosensewebster.com/products/navigation/carto3.aspx, Accessed Oct. 17, 2011, 2011.
- [63] A. Plotkin, O. Shafrir, E. Paperno, and D.M. Kaplan. Magnetic eye tracking: A new approach employing a planar transmitter. *IEEE transactions on bio-medical engineering*, 57(5):1209–1215, March 2010.

-
- [64] R. Iustin, J. Linder, E. Isberg, T. Gustafsson, and B. Lennernäs. A Model Based Positioning System. Patent. WO 2008/079071 A1, World Intellectual Property Organization, 2008.
- [65] W. Yang, C. Hu, M.Q.H. Meng, S. Song, and H. Dai. A Six-Dimensional Magnetic Localization Algorithm for a Rectangular Magnet Objective Based on a Particle Swarm Optimizer. *IEEE Transactions on Magnetics*, 45(8):3092–3099, August 2009.
- [66] J.M. Gilbert, S.I. Rybchenko, R. Hofe, S.R. Ell, M.J. Fagan, R.K. Moore, and P. Green. Isolated word recognition of silent speech using magnetic implants and sensors. *Medical engineering & physics*, 32(10):1189–97, December 2010.
- [67] Y.K. Wang, M.P. Nash, A.J. Pullan, J.A. Kieser, and O. Röhrle. Model-based identification of motion sensor placement for tracking retraction and elongation of the tongue. *Biomechanics and modeling in mechanobiology*, 12(2):383–99, April 2013.
- [68] J.A. Baldoni and B.B. Yellen. Magnetic Tracking System: Monitoring Heart Valve Prostheses. *IEEE Transactions on Magnetics*, 43(6):2430–2432, June 2007.
- [69] H.O. Leira, G.A. Tangen, E.F. Hofstad, T. Langø, and T. Amundsen. A novel in vivo method for lung segment movement tracking. *Physics in medicine and biology*, 57(4):1071–86, February 2012.
- [70] J.T. Sherman, J.K. Lubkert, R.S. Popovic, and M.R. DiSilvestro. Characterization of a Novel Magnetic Tracking System. *IEEE Transactions on Magnetics*, 43(6):2725–2727, June 2007.
- [71] F. Raab, E. Blood, T. Steiner, and H. Jones. Magnetic Position and Orientation Tracking System. *IEEE Transactions on Aerospace and Electronic Systems*, AES-15(5):709–718, September 1979.
- [72] Y. Liu, Y. Wang, D. Yan, and Y. Zhou. DPSD algorithm for AC magnetic tracking system. In *2004 IEEE Symposium on Virtual Environments, Human-Computer Interfaces and Measurement Systems, 2004. (VCIMS).*, pages 101–106. IEEE, 2004.
- [73] P. Ripka, A. Zikmund, and J. Vcelak. Long-range magnetic tracking. In *2012 IEEE Sensors*, pages 1–4. Ieee, October 2012.

- [74] D.D. Arumugam, J.D. Griffin, and D.D. Stancil. Experimental Demonstration of Complex Image Theory and Application to Position Measurement. *IEEE Antennas and Wireless Propagation Letters*, 10:282–285, 2011.
- [75] A. Plotkin and E. Paperno. 3-D magnetic tracking of a single sub-miniature coil with a large 2-D array of uniaxial transmitters. *IEEE Transactions on Magnetics*, 39(5):3295–3297, September 2003.
- [76] O. Shafir, E. Paperno, and A. Plotkin. *Magnetic Tracking with a Flat Transmitter*. Lambert Academic Publishing, 2010.
- [77] S. Joshi and S. Boyd. Sensor Selection via Convex Optimization. *IEEE Transactions on Signal Processing*, 57(2):451–462, February 2009.
- [78] R. Plonsey and D.B. Heppner. Considerations of quasi-stationarity in electrophysiological systems. *The bulletin of mathematical biophysics*, 29(4):657–664, 1967.
- [79] Y. Yan, P.L. Nunez, and R.T. Hart. Finite-element model of the human head: scalp potentials due to dipole sources. *Medical & Biological Engineering & Computing*, 29:475–481, 1991.
- [80] P.H. Schimpf, C. Ramon, and J. Haueisen. Dipole models for the EEG and MEG. *IEEE transactions on bio-medical engineering*, 49(5):409–18, May 2002.
- [81] C. H. Wolters, H. Köstler, C. Möller, J. Härdtlein, L. Grasedyck, and W. Hackbusch. Numerical Mathematics of the Subtraction Method for the Modeling of a Current Dipole in EEG Source Reconstruction Using Finite Element Head Models. *SIAM Journal on Scientific Computing*, 30(1):24–45, January 2008.
- [82] S.P. van den Broek, H. Zhou, and M.J. Peters. Computation of neuromagnetic fields using finite-element method and Biot-Savart law. *Medical & Biological Engineering & Computing*, 34(1):21–26, January 1996.
- [83] F. Edelvik, S. Jakobsson, S. Larsson, M. Persson, and Y. Shirvany. An Improved Method for Dipole Modeling in EEG-Based Source Localization. In *IFMBE Proceedings*, pages 146–149, 2009.
- [84] S. Rush and D.A. Driscoll. EEG electrode sensitivity—an application of reciprocity. *IEEE transactions on bio-medical engineering*, 16(1):15–22, January 1969.

- [85] M. Sun. An efficient algorithm for computing multishell spherical volume conductor models in EEG dipole source localization. *IEEE transactions on bio-medical engineering*, 44(12):1243–52, December 1997.